FFI Norwegian Defence
Research Establishment

23/01196

FFI-RAPPORT

Numerical modelling of short pulse shock initiation of ultrafine Hexanitrostilbene (HNS)

Steinar Børve

Numerical modelling of short pulse shock initiation of ultrafine Hexanitrostilbene (HNS)

Steinar Børve

Norwegian Defence Research Establishment (FFI) 15 September 2023

Keywords
Ammunisjon
Brannrør
Armering
Eksplosiver
Numerisk analyse

FFI report
23/01196

Project number
1645

Electronic ISBN
978-82-464-3491-9

Approvers
Arne Petter Bartholsen, *Director of Research*
Hege Kristin Jødahl, *Research Manager*

The document is electronically approved and therefore has no handwritten signature.

Copyright

Summary

The study of short duration shock pulses is relevant in many high-energetic applications. One such application is the initiation of insensitive high explosives, often preferred as booster charges in military and civilian applications due to superior safety and timing properties. Ultra-fine Hexanitrostilbene (HNS) is a material that meets the requirements of such booster charges. Critical flyer impact velocity for a given flyer thickness and material, and run-up to detonation distance as a function of flyer velocity for a given flyer, becomes key observables in impact experiments designed to characterise a specific grade of HNS. Numerical modelling can serve as an important additional tool in such studies. In this work, we investigate the use of the numerical method smoothed particle hydrodynamics (SPH), and a particular extension to that method called Regularized SPH (RSPH), for modelling the interaction of a plastic flyer with an HNS pellet.

This report describes the basic features of the model used for studying the initiation process of the explosives. It presents a detailed discussion of the importance of using an appropriate amount of artificial viscosity to control numerically the fluctuations resulting from the impact. Details are given on how the Ignition & Growth model describing the detonation process is implemented. Resolution requirements for the specific application is formulated, first for the simpler case of non-reactive HNS, then for reactive HNS. It is concluded that 20-40 calculation nodes (referred to as particles) are needed across the width of the flyer in order to secure a reasonably accurate detonation threshold and run-up to detonation description. This represents a severe resolution requirement which makes it very challenging to simulate the problem in full 3D. Two different options for reducing the CPU-cost, using either variable resolution or a time-varying simulation domain, are discussed. The results indicate that using time-varying simulation domain is a better strategy than using variable resolution in this case because of numerical stability issues.

Comparisons of numerical and experimental results of a 75 μm thick flyer reveal a good fit when the flyer width is roughly 600 μm or larger. As the flyer width is reduced below 600 μm, the numerically obtained critical flyer velocity increases faster than the experimental data suggests. The reason for this discrepancy has as of yet not been established.

Samandrag

Studiar av kortvarige sjokkpulsar er relevant for mange høg-energetiske applikasjonar. Ein slik applikasjon er initieringa av ufølsamt høgeksplosiv, gjerne føretrekt som boosterladning i militære og sivile applikasjonar grunna dei overlegne eigenskapane når det gjeld tryggleik og presisjon i tid. Ultrafin Hexanitrostilbene (HNS) er eit material som oppfyller krava til ein slik boosterladning. Kritisk fart ved anslag på film av spesifisert material og tjukkleik og propageringslengd for trykkbølgje før detonasjon, er viktige markørar i anslagstestar for å kunne karakterisere ein spesifikk variant av HNS. I dette arbeidet undersøker vi bruken av "smoothed particle hydrodynamics" (SPH), og ein spesiell utviding av metoden kalla regularisert SPH (RSPH), til modellering av vekselverknaden mellom ein plastfilm og ein HNS-ladning.

Denne rapporten skildrar dei grunnleggande aspekta ved modellen som skal brukast til å studere initieringsprosessen av eksplosivet. Ein detaljert diskusjon vert presentert av kor viktig det er med riktig bruk av kunstig viskositet for numerisk å kunne kontrollere fluktuasjonane som vert generert som følge av anslaget. Detaljar omkring implementeringa av modellen for detonasjonsprosessen vert gjeven. Krav til oppløysing for den spesifikke applikasjonen vert formulert. Først tek rapporten for seg det enklare problemet med ikkje-reaktivt HNS, for etterpå å sjå på tilfellet med reaktivt HNS. Det vert konkludert med at det trengst 20-40 reknenodar (kalla partiklar) innanfor tjukkleiken til plastfilmen for å få nokolunde riktig detonasjonsterskel og tidsutvikling for tenneprosessen. Dette representerer eit strengt krav til oppløysing som gjer det utfordrande å modellere problemet i full 3D. To ulike strategiar for å redusere CPU-kostnaden vert diskutert, ved bruk av anten variabel oppløysing eller tidsvarierande simuleringsdomene. Resultata indikerer at å bruke tidsvarierande simularingsdomene er ein betre strategi i dette tilfellet enn å bruke variabel oppløysing grunna utfordringar med numerisk stabilitet.

Samanlikning av numeriske og eksperimentelle resultat av ein 75 μm tjukk film syner godt samsvar dersom breidda på filmen er omlag 600 μm eller meir. Dersom breidda er under 600 μm og gradvis vert redusert, aukar den kritiske farten til filmen raskare i dei numeriske simuleringane enn det som vert indikert av dei eksperimentelle resultata. Det er framleis uklart kva som er årsaka til dette avviket.

Contents

Appendix

1 Introduction

Hexanitrostilbene (HNS) is a secondary explosive with favourable safety properties such as high heat resistance and impact insensitivity. In addition, fine-grained varieties such as HNS-IV, can easily be shaped into practical pellets without the need for binders or additives. The list of use includes both military and industrial applications, from detonators and electric foil initiators (EFIs), to aircraft escape systems, space rocket separation systems and charges for deep oil well perforation. HNS is most commonly initiated by a short pulsed shock wave resulting from the impact of a high velocity flyer. The amount of energy needed to detonate an HNS pellet is dependent on how fine-grained the explosive is (Schwarz, 1981). Critical flyer velocity for a given flyer thickness and material, and run-to-detonation distance as a function of flyer velocity for a given flyer, becomes key observables in impact experiments designed to characterise a specific grade of HNS. Numerical modelling can serve as an important additional tool in such studies.

The ignition of a condensed explosive material is a complicated chemical process where shock waves interact with the microstructure of the heterogeneous, energetic material, creating so-called "hot-spots". A wide range of models to describe this process, ranging from detailed, mesoscale models which resolve nanoscale features and require state-of-the-art supercomputers (Yarrington et al., 2018), via stochastic reactive burn models (Kittell, 2020), to deterministic, continuum-based models with experimentally determined parameters linking the macro-and meso-scale physics. The simplest continuum models treat the compression and reaction front as a single front with a prescribed propagation speed (Stewart, 1993). However, the model simplicity is in this case highly restrictive in terms of the physical processes that can reliably be described. A more common approach is therefore to use a kinetic based reaction scheme where the reaction process, although simplified, is treated explicitly. One commonly used kinetic scheme is the so-called Ignition and Growth model[1] (Lee & Tarver, 1980). This model was adapted to the problem of shock pulse initiation of fine-grained HNS in 2014 (Tarver & Chidester, 2014). Although a good fit with experimental data is achieved, it remains an open question to what extent the phenomenological ignition model parameters are method and resolution dependent. In fact, the original paper reveals no details regarding the numerical implementation of the model.

In this report, we apply the I&G model to the case of thin Kapton flyers impacting HNS pellets at high speed. We reexamine the model parameters required to achieve good agreement between experimental data from literature and numerical solutions obtained with the Lagrangian particle method Smoothed Particle Hydrodynamics (SPH) and the related method Regularized SPH (RSPH). In particular, we will investigate the convergence properties of the model and to what extent model modifications can be introduced to ensure good agreement with experimental data at lower resolution levels. The report is organised as follows: In section 2, an introduction to SPH is given. We also briefly look at the material model required for this application, and the I&G model is described, with associated HNS parameters according to (Tarver & Chidester, 2014) listed. Next, in section 3, we take a look at the resolution requirements when simulating thin Kapton flyers impacting non-reactive HNS, as this serves as a simplified first step towards describing the full problem. Section 4 focuses on how the I&G model is implemented in the SPH code. Then, in section 5 the question of resolution requirement is revisited, this time for reactive HNS. Also, modifications to the I&G model parameters for HNS-IV when the flyer thickness is less than 50 μm are discussed. Given the strict resolution requirements formulated in the previous section, strategies for increasing computational efficiency and reducing CPU-cost in multi-dimensional

---

[1] Hereafter referred to as the I&G model

models are of great interest. Section 6 deals with the simulation of thin flyer impact on HNS in 2D and 3D and discusses several possible approaches to tackling this challenge. Appendix A describes a modification to the JWL equation of state used for HNS which improves numerical stability for the low-density case by greatly expanding the regime where the sound speed is well defined.

2 Numerical model

This study is performed using the in-house code REGULUS, a 3D hydrodynamics code based on the Smoothed Particle Hydrodynamics (SPH) method (Gingold & Monaghan, 1977; Monaghan, 2005). REGULUS includes additional algorithms, which are referred to as Regularized SPH (RSPH), which allow for adaptive, time-dependent resolution to be used if necessary (Børve, 2012), and the code has among other things been applied to steel ring fragmentation (Moxnes & Børve, 2015). Initially in this study, the code will be run in a basic mode using only a static, uniform resolution. Only in section 6, will RSPH-specific features be discussed. To facilitate the discussions in this report, we therefore start with a short review of SPH as method.

2.1 Introduction to SPH

Smoothed Particle Hydrodynamics (SPH) is a method that allows a temporal and spatially dependent function $A(\mathbf{r}, t)$ to be estimated in an arbitrary point in space using the following integral interpolant:

$$\overline{A(\mathbf{r}, t)} = \int A(\mathbf{r}', t) W(\mathbf{r} - \mathbf{r}', h) d^3\mathbf{r}', \tag{2.1}$$

where $W(\mathbf{r} - \mathbf{r}', h)$ is an interpolation kernel with an interaction range indicated by the scalar parameter h known as the *the smoothing length*. Common kernels are non-zero only up to a certain multiple of h, for instance 2. In this work, we use the 5th order Wendland kernel (Wendland, 1995). Expressed in terms of normalised distance $\nu = |\mathbf{r}|/h$, the kernel can be written as

$$W_\delta(\nu) = \frac{C_\delta}{h^\delta} \begin{cases} (2-\nu)^4(1+2\nu) & \text{if } 0 \le \nu < 2; \\ 0 & \text{otherwise,} \end{cases} \tag{2.2}$$

where δ is the number of spatial dimensions and C_δ equals $3/64$, $7/(64\pi)$, or $21/(256\pi)$ depending on whether δ is 1, 2, or 3. The Wendland kernel has been shown to have favourable stability properties when used in SPH (Capone et al., 2007).

By discretising the continuous expression in Eq. 2.1, the integral can be transformed into a sum over discrete fluid elements:

$$\overline{A(\mathbf{r}, t)} = \sum_b m_b \frac{A(\mathbf{r}_b, t)}{\rho_b} W(\mathbf{r} - \mathbf{r}_b, h), \tag{2.3}$$

where the quantities m_b and ρ_b are the mass and mass density of fluid element b. In this way, we can estimate the value of the function A at an arbitrary point in space $\mathbf{r}$ based on a set of discrete fluid elements which we from now on will be referring to as *particles*. In order to improve the accuracy of the smooth estimate, one can utilise the unity function, $U(\mathbf{r}, t)$, defined as:

$$U(\mathbf{r}, t) = \sum_b \frac{m_b}{\rho_b} W(\mathbf{r} - \mathbf{r}_b, h). \tag{2.4}$$

A smooth estimate of the function $A(\mathbf{r}, t)$ which is guaranteed to reproduce a constant function is then found by combining Eqs. 2.3 and 2.4

$$\widehat{A(\mathbf{r}, t)} = \frac{\overline{A(\mathbf{r}, t)}}{U(\mathbf{r}, t)}. \tag{2.5}$$

Furthermore, we can estimate the gradient of A, ∇A, by performing the summation using the gradient of the kernel function:

$$\overline{\nabla A(\mathbf{r}, t)} = \sum_b m_b \frac{A(\mathbf{r}_b, t)}{\rho_b} \nabla W(\mathbf{r} - \mathbf{r}_b, h). \tag{2.6}$$

And it is even possible to estimate the Laplacian using the kernel gradient by performing the second derivation using a finite-difference approach:

$$\overline{\nabla^2 A(\mathbf{r}, t)} = 2 \sum_b \frac{m_b}{\rho_b} \frac{A(\mathbf{r}, t) - A(\mathbf{r}_b, t)}{(\mathbf{r} - \mathbf{r}_b)^2} (\mathbf{r} - \mathbf{r}_b) \cdot \nabla W(\mathbf{r} - \mathbf{r}_b, h). \tag{2.7}$$

Since we are now dealing with a discrete description, the accuracy of the results will not only be affected by the smoothing length h, but also on the average particle separation relative to h. In this work, it is standard to use an initial particle separation equivalent to 1.5 particles per h. However, since SPH is a fully Lagrangian method, the particles move with the fluid flow. This causes the particle distribution to be modified during the course of the simulation by the fluid flow. In some cases, this natural flow can lead to an increase in numerical noise because of the discrete nature of the representation.

2.2 Lagrangian formulation of the elastic equations of motion

The code REGULUS is designed to handle fluids both with and without material strength. So for the purpose of generality, we will consider the SPH equations of motion for plastic-elastic materials although material strength is not an important aspect of the current application. Since SPH is a fully Lagrangian method, we formulate the equations of motion using the Lagrangian derivative, $D/Dt = \partial/\partial t + \mathbf{v} \cdot \nabla$. The equations of motion can then be written as

$$\frac{\partial \mathbf{r}}{\partial t} = \mathbf{v}, \tag{2.8}$$

$$\frac{D\rho}{Dt} = -\rho(\nabla \cdot \mathbf{v}), \tag{2.9}$$

$$\frac{D\mathbf{v}}{Dt} = \frac{\sigma}{\rho}, \tag{2.10}$$

$$\frac{De}{Dt} = \frac{1}{\rho} \sigma : \dot{\varepsilon}, \tag{2.11}$$

where ρ is mass density, $\mathbf{v}$ is fluid velocity, e is the internal energy, and $\dot{\varepsilon}$ is the strain rate tensor (defined by Eq. 2.14). The full stress tensor, σ, combines the isothermal pressure, P, and the deviatoric stress tensor $\mathcal{S}$ so that the tensor element with index (k, l) is given as

$$\sigma^{kl} = \mathcal{S}^{kl} - P\delta^{kl}, \tag{2.12}$$

where δ^{kl} is the Kronecker delta function. According to Hooke's law with shear modulus G, the time evolution of $\mathcal{S}$ is found from the additional equation

$$\frac{D\mathcal{S}^{kl}}{Dt} = 2G \left(\dot{\varepsilon}^{kl} - \frac{1}{3} \delta^{kl} \dot{\varepsilon}^{gg} \right) + \mathcal{S}^{kg} \Omega^{gl} - \Omega^{kg} \mathcal{S}^{gl}, \tag{2.13}$$

where the strain rate tensor, $\dot{\varepsilon}$, is given as

$$\dot{\varepsilon}^{kl} = \frac{1}{2}\left(\frac{\partial v_k}{\partial r_l} + \frac{\partial v_l}{\partial r_k}\right) \tag{2.14}$$

and

$$\Omega^{kl} = \frac{1}{2}\left(\frac{\partial v_k}{\partial r_l} - \frac{\partial v_l}{\partial r_k}\right) \tag{2.15}$$

is the rotation rate tensor. In addition to Eqs. 2.9-2.15, we require an equation of state (EOS) which links ρ, P, and if applicable, e together. On top of this, one can build models to describe plastic and brittle behaviour in the material.

2.3 SPH equations of elastic motion

In this section, we transform the equations given in 2.2 into a set of solvable SPH equations of motion based on the method defined by Eqs. 2.3 and 2.6 (Monaghan, 2005). Hereafter, we simplify the notation so that for particles a and b we have

$$\begin{aligned}
A_a &= A(\mathbf{r}_a, t), && (2.16)\\
\mathbf{r}_{ab} &= \mathbf{r}_a - \mathbf{r}_b, && (2.17)\\
\hat{\mathbf{r}}_{ab} &= \frac{\mathbf{r}_{ab}}{|\mathbf{r}_{ab}|}, && (2.18)\\
\mathbf{v}_{ab} &= \mathbf{v}_a - \mathbf{v}_b, && (2.19)\\
h_{ab} &= \frac{1}{2}\left(h_a + h_b\right), && (2.20)\\
W_{ab} &= W(\mathbf{r}_{ab}, h_{ab}) && (2.21)
\end{aligned}$$

and

$$\nabla_a W_{ab} = \nabla_a W(\mathbf{r}_{ab}, h_{ab}). \tag{2.22}$$

Individual vector components are indicated by a second, lower index, e.g. the kth component of the velocity of particle a is written $v_{a,k}$, and the kth component of the kernel gradient vector for the particle pair a and b (differentiated with respect to the position of a) is written $\partial_k W_{ab}$ for short. In addition, since a Lagrangian formulation is given, we hereafter replace the use of D/Dt by simply d/dt.

The SPH equations of motion can then be written as follows:

$$\begin{aligned}
\frac{d\mathbf{r}_a}{dt} &= \mathbf{v}_a - \chi \sum_b m_b \frac{\mathbf{v}_{ab}}{\rho_{ab}} W_{ab}, && (2.23)\\
\frac{d\rho_a}{dt} &= \rho_a \sum_b \frac{m_b}{\rho_b} \mathbf{v}_{ab} \cdot \nabla_a W_{ab}, && (2.24)\\
\frac{dv_{a,k}}{dt} &= \sum_b m_b \left(\frac{\sigma_a^{kl}}{\rho_a^2} + \frac{\sigma_b^{kl}}{\rho_b^2} + R_{ab}^{kl} f^n - \Pi_{ab}\right) \partial_l W_{ab}, && (2.25)\\
\frac{de_a}{dt} &= -\frac{1}{2} \sum_b m_b v_{ab,k} \left(\frac{\sigma_a^{kl}}{\rho_a^2} + \frac{\sigma_b^{kl}}{\rho_b^2} + R_{ab}^{kl} f^n - \Pi_{ab}\right) \partial_l W_{ab} \\
&\quad - \sum_b \frac{m_b}{\rho_b} \Upsilon_{ab} \hat{\mathbf{r}}_{ab} \cdot \nabla_a W_{ab}, && (2.26)
\end{aligned}$$

where Eq. 2.25 includes a summation over the index l and Eq. 2.26 includes a double summation over both k and l.

In this numerical formulation, particles are moved with a velocity that deviates slightly from the fluid flow, as indicated by the second term of Eq. 2.23. The parameter χ is normally set to 0.5 which is also its maximum value. The formulation also includes terms of artificial dissipation and stress. The repulsive force term, $R_{ab}^{kl} f^n$, is used to avoid (or at least reduce the growth rate of) the so-called tensile instability (Monaghan, 2000), but is not important in the current application. The artificial viscosity, represented by the term Π_{ab}, is important in the description of shock waves. It helps to resolve shock fronts and to reduce numerical noise. The last term in the energy equation describes the artificial conductivity. It contributes to an improved description of contact discontinuities. In the simulations of shock-wave initiated high explosives, finding the right level of artificial dissipation is particularly important.

2.3.1 Artificial dissipation (AD) in SPH

For the artificial viscosity (AV), denoted Π, the following formulation is chosen:

$$\Pi_{ab} = \begin{cases} \frac{(\beta_{ab}\mu_{ab} - \alpha_{ab}c_{ab})\mu_{ab}}{\rho_{ab}} & \text{if } \mu_{ab} < 0; \\ 0 & \text{otherwise,} \end{cases} \tag{2.27}$$

where the parameter

$$\mu_{ab} = \frac{h_{ab}\mathbf{v}_{ab} \cdot \mathbf{r}_{ab}}{r_{ab}^2 + \epsilon^2 h_{ab}^2} \tag{2.28}$$

is roughly equal to the relative velocity between particles a and b when the separation between them is comparable to h_{ab}, the mean smoothing length for the pair. When the inter-particle distance is decreased, the absolute value of μ_{ab} increases. A potential singularity at $r_{ab} = 0$ is avoided by choosing $\epsilon > 0$. Typically, ϵ is chosen to be 0.1. In Eq. 2.27, c_{ab} and ρ_{ab}, represent the mean sound speed and density, respectively, of the particle pair a and b. The last two parameters, α_{ab} and β_{ab}, are non-physical terms that determine the strength of the artificial viscosity. Traditionally, these terms are constants, common values in shock wave problems are $\alpha = 1$ and $\beta = 2$)(Monaghan & Gingold, 1983). To better restrict the use of AV to areas where it is needed, α and β can be turned into particle properties.

In REGULUS, a slight generalisation of the approach described by Morris & Monaghan (1997) is chosen. The evolution of α_a is given as

$$\frac{d\alpha_a}{dt} = -\frac{\alpha_a - \alpha_{\min}}{\tau_a} + A\left(\frac{\alpha_{\max} - \alpha_a}{\alpha_{\max}}\right)^{\kappa} \mathcal{S}_a, \tag{2.29}$$

where the source term is given as

$$\mathcal{S}_a = \max[-(\nabla \cdot \mathbf{v})_a, 0] \tag{2.30}$$

and the decay timescale, τ_a, is

$$\tau_a = \frac{h_a}{C v_{\mathrm{sig}}, a} \tag{2.31}$$

with C being a dimensionless constant (commonly chosen to be 0.1) and

$$v_{\mathrm{sig},a} = \max_b[c_{ab} - 2\mathbf{v}_{ab} \cdot \hat{\mathbf{r}}_{ab}]. \tag{2.32}$$

Default values are $\alpha_{\text{min}} = 0$, $\alpha_{\text{max}} = 1$, $A = 1$ and $\kappa = 1$. The latter parameter will be kept at its default value in this work, while the other 3 parameters are optimised for the current application in section 3.1. As a general remark, it can be said that the exponent κ should in any case be an odd integer so that the source term becomes anti-symmetric. The parameter β_a is set equal to $2\alpha_a$, as is commonly done.

The contribution of particle b on the artificial conductivity (AC) of particle a is determined by the quantity denoted Υ_{ab} which can expressed as

$$\Upsilon_{ab} = \lambda_a u_{\text{sig},ab}(e_a - e_b) \tag{2.33}$$

according to Price (2008). The signal velocity in this case, $u_{\text{sig},ab}$, is not linked to the physical signal velocity, but rather to pressure variation and is given as

$$u_{\text{sig},ab} = \sqrt{\frac{|P_a - P_b|}{\rho_{ab}}}. \tag{2.34}$$

Note that in situations where external forces, such as gravity, are significant the pressure terms appearing in Eq. 2.34 should be deviations from equilibrium pressure. The parameter λ_a plays a similar role in the AC as α_{ab} serves in the AV. It could be a constant. However, it is recommended that it instead is a particle property which varies in time according to a decay equation of the same type as written in Eq. 2.29 with the same decay time τ_a:

$$\frac{d\lambda_a}{dt} = -\frac{\lambda_a - \lambda_{\text{min}}}{\tau_a} + A_u \left(\frac{\lambda_{\text{max}} - \lambda_a}{\lambda_{\text{max}}}\right)^{\kappa_u} \mathcal{S}_{u,a}, \tag{2.35}$$

However, a different source term is proposed (Price, 2008):

$$\mathcal{S}_{u,a} = \max\left[\frac{h_a|\nabla^2 e|_a}{\sqrt{e_a + \epsilon^2 c_a}}, 0\right]. \tag{2.36}$$

Default values are chosen consistently with the artificial viscosity parameters: $\lambda_{\text{min}} = 0$, $\lambda_{\text{max}} = 2$, $A_u = 1$ and $\kappa_u = 1$ (κ_u must be an odd integer). Again, appropriate values for these parameters in the current application are discussed in section 3.1.

2.4 Material models

The current application includes two materials. The flyer is assumed to be made of Kapton®, while the pellet is made of HNS-IV. The equation of state (EOS) of Kapton is assumed to be given by the Grüneisen equation (Lemons & Lund, 1999)

$$P = \frac{\rho_0 C_0^2 \eta \left(1 - \frac{\gamma_0}{2}\eta\right)}{(1 - s\eta)^2} + \gamma_0 \rho e, \tag{2.37}$$

where $\eta = 1 - \rho_0/\rho$ and with the following model parameters: $\rho_0 = 1.414$ g/cm^3, $C_0 = 2.737$ km/s, $\gamma_0 = 0.76$, and $s = 1.41$ (Tarver & Chidester, 2014)[2]. As far as material strength is concerned, we use a parametric strength model where the assumed tensile stress-strain curve is given by Fig. 1 of Dupont (2021).

---

[2] As commonly assumed, the relationship between shock velocity U_s and particle velocity u_p is then $U_s = C_0 + su_p$.

2.4.1 HNS-IV EOS

For the HNS-IV pellet, we use the EOS model proposed in Tarver & Chidester (2014), albeit with a small modification in the low-density regime. The model in Tarver & Chidester (2014) is based on the Jones-Wilkins-Lee (JWL) EOS which is commonly used for condensed phase explosives. According to this equation, the pressure is given as

$$P = A\left(1 - \frac{\omega\mu}{R_1}\right)e^{-R_1/\mu} + B\left(1 - \frac{\omega\mu}{R_2}\right)e^{-R_2/\mu} + \omega\mu(\rho e + E_0), \tag{2.38}$$

where $\mu = \rho/\rho_0$ is normalized density, and the parameters A, B, R_1, R_2, ω and E_0 are determined experimentally. To achieve a more compact notation later on, we formulate the JWL EOS using the functions $G(\mu)$ and $H(\mu)$, where

$$G(\mu) = A\left(1 - \frac{\omega\mu}{R_1}\right)e^{-R_1/\mu} + B\left(1 - \frac{\omega\mu}{R_2}\right)e^{-R_2/\mu} + \omega\mu E_0 \tag{2.39}$$

and

$$H(\mu) = \omega\mu \tag{2.40}$$

making it possible to write

$$P = G(\mu) + H(\mu)\rho e. \tag{2.41}$$

In this particular application, two separate JWL equations are used, one for unreacted HNS and one for reacted HNS. The JWL parameters for the two states according to Tarver & Chidester (2014) are listed in Table 2.1. The equilibrium density of HNS-IV, ρ_0, is assumed to be $\rho_0 = 1.6$ g/cm^3.

Table 2.1 JWL EOS parameters for unreacted and reacted HNS-IV according to Tarver & Chidester (2014).

Parameter	A (GPa)	B (GPa)	R_1	R_2	ω	E_0 (GPa)
Unreacted	$3.318 \cdot 10^4$	-2.5154	11.5	1.15	0.5675	0
Reacted	536.25	27.02	5.4	1.8	0.45	7.0

With the use of the I&G model, SPH particles can be partially ignited since on a given location, there might be a mixture of both reacted and unreacted HNS. It must therefore be possible to describe a gradual change from the unreacted to the reacted EOS state. This implies that in regions where HNS has partially reacted, the two equations need to be combined. This is achieved by assuming pressure equilibrium which means that reacted and unreacted components occupying the same region in space have the same pressure but different temperatures. This means that there are separate versions of Eqs. 2.38-2.40 for each of the two components, with P being the same. The generalised method for N_s components, where each component i has a mass fraction of α_i is described in Clutter & Belk (2002). The total, specific thermal energy can then be written as a weighted sum of the specific thermal energy of each component

$$\rho e = \sum_i \alpha_i \rho e_i. \tag{2.42}$$

We use Eq. 2.41 to find ρe_i as function of P and μ which makes it possible to express ρe as

$$\begin{aligned}\rho e &= P\sum_i \frac{\alpha_i}{H_i(\mu)} - \sum_i \frac{\alpha_i G_i(\mu)}{H_i(\mu)} && (2.43)\\ &= P\sum_i s_i(\mu) - \sum_i s_i(\mu)G_i(\mu), && (2.44)\end{aligned}$$

where we have introduced the quantity $s_i(\mu)$ defined as

$$s_i(\mu) = \frac{\alpha_i}{H_i(\mu)}. \tag{2.45}$$

If we also define $S(\mu)$ as the sum

$$S(\mu) = \sum_i s_i(\mu) \tag{2.46}$$

the pressure can easily be written as

$$P = \frac{1}{S(\mu)}\left[\rho e + \sum_i s_i(\mu)G_i(\mu)\right]. \tag{2.47}$$

An expression for the sound speed, C_s can be calculated directly from the definition

$$C_s^2 = \frac{dP}{d\rho} \tag{2.48}$$

in combination with the second law of thermodynamics which gives us

$$\frac{\partial e}{\partial \rho} = \frac{P}{\rho^2}. \tag{2.49}$$

This gives us the following expression for the sound speed squared in the mixed-JWL case:

$$C_s^2 = \frac{1}{\rho S(\mu)}\left[P(2S(\mu)+1) - 2\sum_i s_i(\mu)G_i(\mu)\right] + \frac{1}{\rho_0 S(\mu)}\sum_i \frac{\partial G_i(\mu)}{\partial \mu}. \tag{2.50}$$

Although a flyer-induced shock wave primarily acts to compress the target HNS pellet, there are situations where the outer parts of the pellet can experience a substantial expansion after the initial shock has propagated through the region in question. This could for instance be the case for SPH pellet particles interacting directly with a very thin flyer. Although this might to some extent be due to numerical inaccuracies, it must be taken into account that the density for individual SPH pellet particles might fall well below the HNS equilibrium density. The JWL EOS, with the parameters chosen for unreacted HNS-IV, is not well suited for handling these situations. Depending on the level of thermal energy, the pressure starts to increase with decreasing density when μ is around 0.8 or so resulting in the sound speed becoming imaginary in this regime. This problem is discussed in some detail in Appendix A.1. A low-density correction to the JWL EOS is proposed in section A.2 to avoid unphysical sound speed in the rare occasions when density falls well below of the equilibrium density. The corrected EOS is used for HNS-IV in this work.

2.5 The Ignition and Growth model

2.5.1 Model theory

The Ignition and Growth (I&G) model is a Zeldovich-von Neumann-Doring (ZND) model where the detonation front is treated as a discontinuity while explicitly modelling the reaction process behind the shock (Lee & Tarver, 1980). It is formulated as a reaction rate expression of the reacted fraction, F, where the total reaction rate is split into three parts:

$$\frac{dF}{dt} = \frac{dF_0}{dt} + \frac{dF_1}{dt} + \frac{dF_2}{dt}. \tag{2.51}$$

As described by e.g. Kury et al. (1999), the three terms correspond to the three reaction stages typically observed in shock initiation and detonation of heterogeneous, condensed explosives. Each term only contributes to the total reaction rate when specific conditions are met.

The first term accounts for the near immediate ignition of a relatively small amount of the explosives due to the initial shock compression and is expressed as

$$\frac{dF_0}{dt} = I(1-F)^b(\frac{\rho}{\rho_0} - 1 - a)^X, \tag{2.52}$$

if $\rho/\rho_0 > 1 + a$ and $0 < F < F_{0,\max}$. The second term represents the intermediate stage of rapid exothermic decomposition of the explosives into product gases, while the third term models the diffusion controlled formation of carbon species. The second term is written as

$$\frac{dF_1}{dt} = G_1(1-F)^c F^d P^y \tag{2.53}$$

if $P > 0$ and $0 < F < F_{1,\max}$, and the third is correspondingly given as

$$\frac{dF_2}{dt} = G_2(1-F)^e F^g P^z \tag{2.54}$$

if $P > 0$ and $F_{2,\min} < F < 1$.

2.5.2 Parameters for HNS-IV based on literature

We review the I&G model parameters used in Tarver & Chidester (2014) for modelling shock initiation of HNS. All 15 parameters are listed in Table 2.2. The most important parameters in controlling the sensitivity of the modelled explosives are G_1, G_2, and $F_{0,\max}$.

Table 2.2 Ignition and Growth parameters for HNS-IV according to Tarver & Chidester (2014).

Term	Parameter	Value	Unit
1	I	$1.4 \cdot 10^6$	μs^{-1}
	b	0.667	-
	a	0.2669	-
	X	4.0	-
	$F_{0,\text{max}}$	0.08 (0.18†)	-
2	G_1	0.37	$\text{GPa}^{-2}\mu s^{-1}$
	c	0.667	-
	d	0.667	-
	y	2	-
	$F_{1,\text{max}}$	1.0	-
3	G_2	0.0148	$\text{GPa}^{-3}\mu s^{-1}$
	e	0.667	-
	g	0.667	-
	z	3	-
	$F_{2,\text{min}}$	0.0	-

†Applies to flyer thickness less than 20 μm (see discussion in section 5.2).

3 Flyer impact on non-reactive HNS pellets

We will start by looking at a series of tests performed with non-reactive HNS pellets. This means that the ignition modelling is turned completely off, while the remaining HNS material properties are the same as in the reactive case. Since an inert pellet is inherently stable in a way that an explosive pellet is not, flyer impact on an inert pellet represents a much simpler problem than the corresponding impact on an explosive pellet. A numerical model that is meant to describe flyer-induced ignition of an explosive pellet should therefore, as a starting point, provide an accurate description of the corresponding process with an inert pellet. By not having to consider the ignition processes, we can more easily investigate the effect of the numerical resolution and artificial dissipation (AD) settings. The two topics are clearly related, but we will first focus on the artificial dissipation settings. Once we have determined the optimal level of AD for the current application, we look in more detail on convergence in order to formulate a resolution criteria in the inert case. The resolution criteria in the explosive case is expected to be at least as strict as in the inert case, possibly stricter.

3.1 Optimizing the artificial dissipation (AD) implementation for flyer impacts on HNS pellets

As explained in section 2.3.1, AD is used in the numerical model in order to resolve shock fronts and to prevent unwanted oscillations in the post-shock state. An unwanted side effect can be that the dissipation also dampens important physical features. This motivates the use of the switching techniques described in section 2.3.1 in order to only apply AD close to the shock front itself. The reaction rate described by the I&G model (see section 2.5) initially depends primarily on the pressure and, in the initial phase, on the mass density. Oscillations in pressure or density due to numerical artefacts could therefore cause the explosive material sensitivity to be overestimated. On the other hand, unnecessarily high dissipation could quench run-up processes which in reality should lead to detonation. Choosing the right algorithm and level of AD is therefore crucial to getting an accurate numerical description of shock-induced initiation processes.

3.1.1 AD Simulation setups

In this section we will compare results obtained with static artificial dissipation (SAD) and variable artificial dissipation (VAD). In all, we will look at 4 different parameter settings in each category. In all cases, the conductivity parameters are identical to the viscosity parameters. In the SAD case, we will consider the values 0.1, 0.2, 0.5, and 1.0 for the two parameters α_a and λ_a. Solutions obtained with these AD settings will be referred to as SAD01, SAD02, SAD05, and SAD10. When VAD is applied, the time-derivatives of α_a and λ_a are calculated as described in 2.3.1, with the amplitudes, A and A_u, set to 1, 3, 5, 10. The exponents κ and κ_u is set to the default value of 1. Solutions obtained with these AD settings will be referred to as VAD01, VAD03, VAD05, and VAD10.

We simulate the following combinations of flyer thickness (d) and flyer velocity (v_f), d = 25 μm with v_f = 2.7 km/s, d = 50 μm with v_f = 2.2 km/s, d = 100 μm with v_f = 1.7 km/s, and finally d = 200 μm with v_f = 1.5 km/s. The flyer velocity is in each case chosen equal to the estimated critical velocity for the initiation of HNS, listed in Table 5.1. All simulations are run for a fairly short time period of 0.4 μs. The resolution in all simulations to be evaluated is uniform and given as $d/\Delta = 160$, where $\Delta = h/1.5$ is the initial particle separation and h is the smoothing length. In lack of experimental or alternative theoretical results to compare with, a reference solution for each combination of flyer thickness and flyer velocity is constructed based on simulation results using SAD with $\alpha_a = \lambda_a = 0.1$ and the resolution $d/\Delta = 1280$, Choosing a very low SAD level ensures that important features are not damped, but it also causes the oscillations near the shock front to be quite severe. To remove much of the unwanted oscillations from the reference solutions, a post-processing filtering is applied to the post-shock reference data.

3.1.2 AD pressure profile comparison

We will evaluate different numerical results by comparing data obtained on virtual pressure sensors located 0.02 mm, 0.3 mm, 0.5 mm 0.7 mm and 0.9 mm into the pellet (relative to the impact surface). First, we make direct comparisons of the temporal profiles for sensors 1 (0.02 mm) and 4 (0.7 mm) for flyer thickness $d = 25$ μm and $d = 200$ μm. The profiles are plotted in Fig. 3.1, where panels **a** and **b** show the $d = 25$ μm results for sensors 1 and 4, respectively. Panels **c** and **d** show the corresponding results for $d = 200$ μm. The line colour identifies the different AD solutions: SAD01 (yellow), SAD02 (orange), SAD05 (red), and SAD10 (green), VAD01 (blue), VAD03 (brown), VAD05 (grey), and VAD10 (black). The black, dashed line shows the filtered, high resolution reference solution. The pressure unit is GPa and the time unit is μs.

Fig. 3.1a illustrates the strong post/shock oscillations which are present when the AD level is low. In SAD01, the amplitude of the oscillations is initially around 30 % compared to the reference solution. Increasing the dissipation parameter from 0.1 to 0.5 (SAD05) decreases the amplitude of the oscillations to roughly 10 %. It also decreases the average pressure level by a few percentage. Increasing the static dissipation parameter to 1.0 (SAD10) forces the pressure profile to stay below the reference pressure more or less through the whole time series. The trend is much the same when using a variable AD, although the damping of oscillations at later times is less pronounced than in the static case. This is reasonable since the VAD algorithm causes the AD strength near the shock front to decrease as the shock is weakened with time. The initial damping is slightly larger in VAD01 than in SAD02, and slightly larger in VAD10 than in SAD05.

From the sensor 4 results for $d = 25$ μm case (see Fig. 3.1b), we see that the oscillations in pressure is not the most distinct feature separating the various numerical solutions. Instead, we notice the differences in shock arrival time between the different solutions. Based on the recorded shock arrival times, we can estimate the average shock speed between sensors 1 and 4 to be 3250 m/s in the reference solution. In SAD10, the shock arrives about 3 ns earlier than in the reference solution, which corresponds to roughly 1.5% larger average shock speed than in the reference solution. For SAD05 and VAD10, the shock arrival times are about 2 ns smaller than the reference arrival time, a 1.0% larger average shock speed than in the reference solution.

The two lower panels, panels **c** and **d**, show the corresponding sensor data for the case $d = 200$ μm. Again, the oscillation amplitude for sensor 1 is very large if the AD level is too low. With increased AD, static or variable, these oscillations decrease in amplitude. In this case, this applies to both sensors. There is another prominent feature of the sensor 1 profiles which needs to be addressed: the pressure spike occurring about 0.02 μs after the shock arrives. The spike, which is much sharper in the reference solution, is only weakly affected by the AD settings. It is caused by a well-known deficiency in momentum-conserving SPH formulations related to contact discontinuities, in particular in relation to material interfaces. The artificial pressure spike coincides with the interface between the flyer material on the left and the pellet material on the right. It could represent a problem in the modelling of the ignition process, but only for flyers thicker than 75 μm.

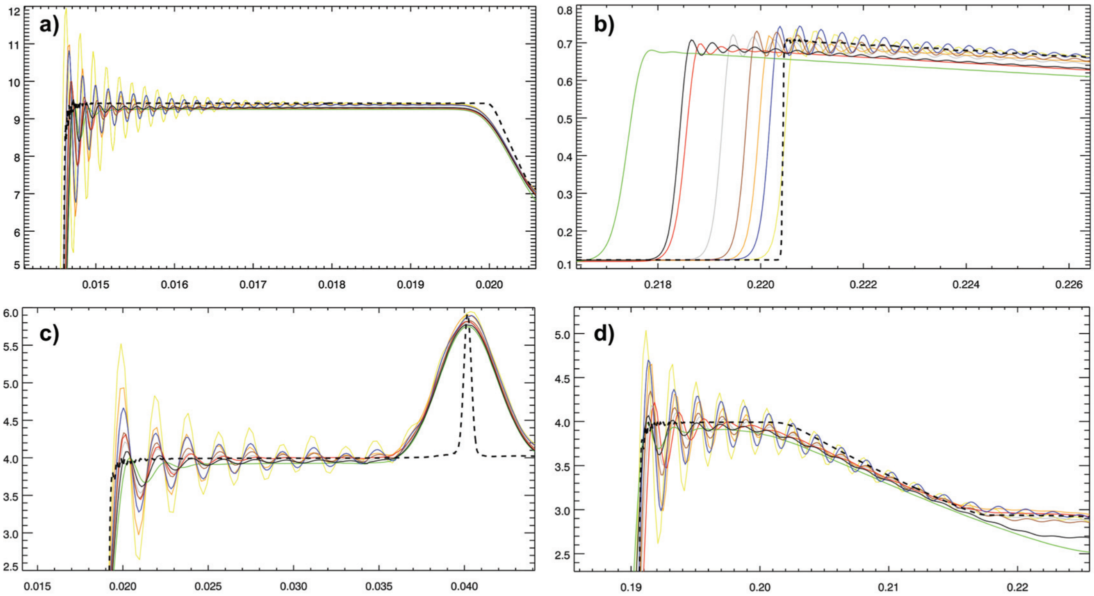

Figure 3.1 *Recorded pressure profiles (in units of GPa) as functions of time (in units of μs) in the SAD01 (yellow), SAD02 (orange), SAD05 (red), and SAD10 (green), VAD01 (blue), VAD03 (brown), VAD05 (grey), and VAD10 (black) solutions. The simulated flyer thickness is $d = 25\ \mu m$ (panels* **a** *and* **b***) and $d = 200\ \mu m$ (panels* **c** *and* **d***), and results are shown for sensors 1 (panels* **a** *and* **c***) and 4 (panels* **b** *and* **d***). The black, dashed line indicates the filtered, high resolution reference solution.*

3.1.3 Sensor accuracy as a function of AD settings

Next, we want to investigate the sensor data accuracy as a function of the AD settings in more detail, and we assume that the high resolution, reference solutions can be considered to be of high accuracy. Let $P_s^{\mathrm{ref}}(t)$ denote the reference pressure profile at sensor location s and assume that the primary shock front is first registered at this location at time t_s^{ref}. This can be defined as the largest time t_s^{ref} of which the following condition is true:

$$P_s^{\mathrm{ref}}(t) < P_{\mathrm{trig}} \text{ for } t < t_s^{\mathrm{ref}}. \tag{3.1}$$

Peak reference pressure, defined as the maximum pressure over the entire pressure series, is denoted $P_{s,M}^{\mathrm{ref}}$. We define $P_s(t)$, $P_{s,M}$ and t_s for any solution that we want to evaluate (hereafter referred to as the test solution). Based on these observables, we want to define 3 error indicators, $e_{s,a}$, $e_{s,M}$ and δt_s, for a given sensor location s.

The first error indicator, $e_{s,a}$, measures the average difference between the pressure profiles in the test solution and the reference solution in the time period $t_s \leq t_k \leq 0.4$ μs, where t_k is time sample k in the test solution. Let us assume that $t_s \leq t_k$ for $k \geq k_s$. Then $e_{s,a}$ is defined as

$$e_{s,a} = \sqrt{\frac{\sum_{k=k_s}[P_s^{\mathrm{ref}}(t_k) - P_s(t_k)]^2}{\sum_{k=k_s} P_s^{\mathrm{ref}}(t_k)^2}}. \tag{3.2}$$

The second indicator looks at the difference in peak pressure as this is very important to the ignition model. It is defined as

$$e_{s,M} = \frac{|P_{s,M}^{\mathrm{ref}} - P_{s,M}|}{P_{s,M}^{\mathrm{ref}}}. \tag{3.3}$$

The last indicator measures simply the difference in shock arrival time between the reference solution and a test solution. It is defined as

$$\delta t_s = |t_s - t_s^{\mathrm{ref}}|. \tag{3.4}$$

These sensor specific indicators can then be averaged over all $N_s = 5$ sensors in the simulations:

$$E_a = \frac{1}{N_s}\sum_{s=1}^{N_s} e_{s,a}, \tag{3.5}$$

$$E_M = \frac{1}{N_s}\sum_{s=1}^{N_s} e_{s,M} \tag{3.6}$$

and

$$\Delta T = \frac{1}{N_s}\sum_{s=1}^{N_s} \delta t_s. \tag{3.7}$$

Fig. 3.2 shows the sensor averaged error indicators for flyer thickness $d = 50$ μm for all tested AD settings. From left to right on the horizontal axis the errors in SAD01, SAD02, SAD05, SAD10, VAD01, VAD03, VAD05, and VAD10 are shown [3]. The average error in pressure (E_a) is relatively

---

[3] Regarding the notation on the horizontal axis: the floating points refer to the value of $\alpha = \lambda$ in the simulations with SAD settings (SAD01-SAD10), while the tick names starting with the letter 'V' refer to simulations run in VAD mode with $\kappa = \kappa_u = 1$ and the amplitudes, A and A_u, set to 1, 3, 5, 10 (VAD01-VAD10).

small in simulations with static AD if the AD level is low. This is because the solutions mostly oscillate around the correct solution with negligible phase error, while the error in peak pressure (E_M) is large because the oscillation amplitude is quite large. The shock arrival time error (ΔT) is low, which confirms that the phase error is small. As the static AD level is increased, we see that the error E_M clearly decreases due to the increased smoothing effect caused by the dissipation. On the other hand, E_a only exhibits a very small decrease before starting to increase. This is because the decrease in error due to the post-shock oscillations is quickly more than compensated by increased error due to the error in the shock arrival time.

A similar trend is seen in the solutions with variable AD when the source amplitudes, A and A_u, increase from 1 to 10. The average pressure error indicator, E_a, is at its smallest when A and A_u are small, but the difference between the 4 VAD solutions in the graph is only about 20%. Peak pressure error, on the other hand, drops by almost a factor 10 as the source amplitudes increase from 1.0 to 10.0. The shock arrival time error increases moderately with increasing source amplitude. When $A = A_u = 1.0$, the effective AD level is quite small. For the $d = 50$ μm case, the viscosity parameter α reaches a global maximum of just over 0.3. This occurs at the flyer-pellet interface right after impact. With time, the peak in α tracks the shock front location but drops off in magnitude. The overall maximum of the conductivity parameter λ is about twice as large as that of α, but it drops off more quickly with time. It is therefore reasonable to expect the VAD01 solution to have characteristics somewhere between that of SAD02 and SAD05. If the source amplitudes are increased to 5.0, the maximum values of α and λ are around 0.8 and 0.9, respectively. And for $A = A_u = 10.0$, both parameters reach a global maximum of around 0.9-0.95. Halfway through the simulation (at 0.2 μs), peak value of α is still around 0.65 while the peak value of λ has dropped to around 0.25. This causes the characteristics of VAD10 to be somewhere between that of SAD05 and SAD10.

Finally, we want to summarise our findings about the effect of changing the AD settings. The error indicators are functions of the AD settings chosen. Let us express this dependence by writing the indicators as $E_a(i)$, $E_M(i)$ and $\Delta T(i)$, where the index i refers to the solution with a specific AD setting. In order to compare the three indicators directly, we normalise them by the corresponding maximum values to get

$$e_a(i) = \frac{E_a(i)}{\mathrm{Max}_i[E_a(i)]}, \tag{3.8}$$

$$e_M(i) = \frac{E_M(i)}{\mathrm{Max}_i[E_M(i)]} \tag{3.9}$$

and

$$\delta t(i) = \frac{\Delta T(i)}{\mathrm{Max}_i[\Delta T(i)]}. \tag{3.10}$$

Based on these normalised error indicators, we can construct the combined error indicator $e_S(i)$ defined as

$$e_S(i) = (e_a(i) + e_M(i) + \delta t(i)) \cdot \mathrm{Max}([e_a(i), e_M(i), \delta t(i)]). \tag{3.11}$$

Fig. 3.3 shows $e_S(i)$ as function of the AD settings, which from left to right on the horizontal axis is SAD01, SAD02, SAD05, SAD10, VAD01, VAD03, VAD05, and VAD10. Results are shown for all 4 simulated flyer thickness values, $d = 25$ μm (black line), $d = 50$ μm (brown line), $d = 100$ μm (green line), and $d = 200$ μm (blue line). Although there is some differences in the curves, the main trend is the same irrespective of flyer thickness. If static AD is chosen, $\alpha = \lambda = 0.5$ is preferable to very small values or values close to unity. However, choosing a variable AD with source amplitudes

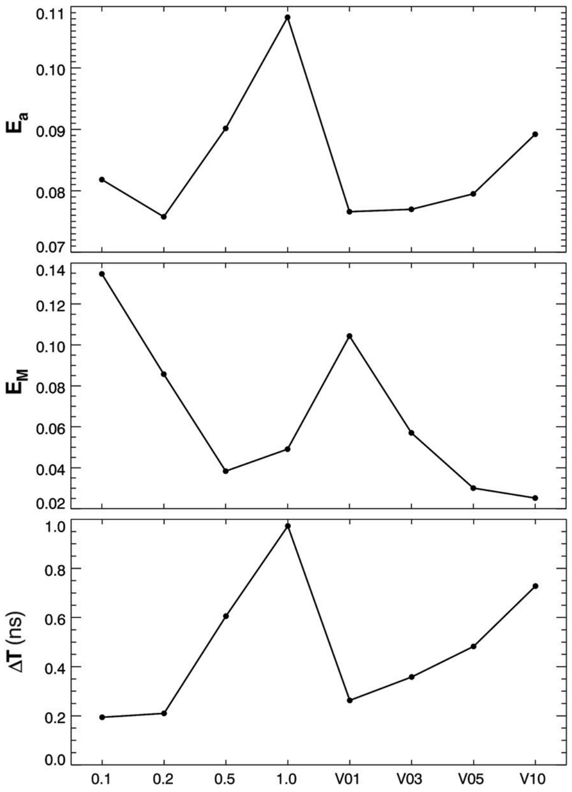

Figure 3.2 *Sensor averaged error indicators, E_a (panel* **a***), E_M (panel* **b***) and ΔT (panel* **c***) for the d = 50 μm as functions of the AD settings. From left to right on the horizontal axis the errors in SAD01, SAD02, SAD05, SAD10, VAD01, VAD03, VAD05, and VAD10 are shown.*

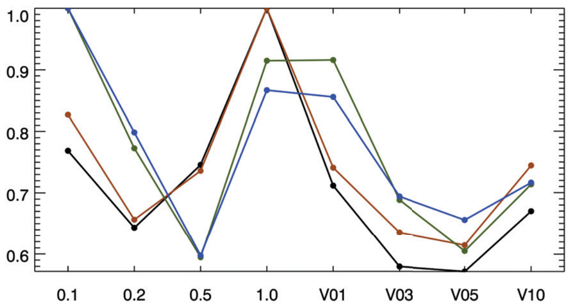

Figure 3.3 Combined error indicator, e_S, for flyer thickness d = 25 μm (black), d = 50 μm (brown), d = 100 μm (green), and d = 200 μm (blue line) as function of the AD settings. From left to right on the horizontal axis the errors in SAD01, SAD02, SAD05, SAD10, VAD01, VAD03, VAD05, and VAD10 are shown.

around 5 appears to be better still. In particular, this is true for the smallest simulated flyer thickness, $d = 25$ μm, which is considered the most challenging to model. For the rest of this work, we therefore choose a variable AD setting with source amplitudes set to $A = A_u = 5.0$ and with source exponents $\kappa = \kappa_u = 1$.

3.2 Resolution requirements for simulations of flyer impact on inert HNS

Once the optimal AD settings for the current application has been determined, we should investigate the effect of varying the resolution in more detail. The same approach as for the AD analysis is chosen here. We compare sensor data obtained at different resolution, with the reference solutions defined in section 3.1.3. Fig. 3.4 shows the time-dependent pressure at sensor point 1, located 0.02 mm from the impact surface into the pellet. Results are shown for flyer thickness 25 μm (panel **a**), 50 μm (panel **b**), 100 μm (panel **c**), and 200 μm (panel **d**). The resolution is given by the ratio of flyer thickness (d) to particle size (Δ) and is equal to 5 (pink curves), 10 (yellow curves), 20 (orange curves), 40 (red curves), 80 (green curves), 160 (blue curves), 320 (brown curves), 640 (grey curves), and 1280 (black curves). The black, dashed curves indicate the filtered, high resolution reference solution. A simple inspection of the curves reveals that $d/\Delta \geq 40$ will give consistent pressure levels in the shocked material. Increasing the resolution further will make the shocks sharper and reduce the fluctuations in the post-shock phase. Qualitatively, it is quite clear that the solutions converge.

In order to quantify the effect of changing the resolution, the error estimates defined in section 3.1.3 is used: E_a (average error in pressure), E_M (error in peak pressure), and ΔT (error in shock time-of-arrival). Fig. 3.5 shows the error functions for the case $d = 50$ μm. The first error function, E_a , shown in panel **a**, exhibits a very smooth decrease with increasing d/Δ. The fact that E_a decreases by just over a factor 10 when d/Δ increases by more than 100 could indicate a fairly slow convergence. E_M, has a clear shift in trend at $d/\Delta = 40$, in contrast to what was seen with E_a. For $d/\Delta > 40$, the peak error changes very little, while for smaller values of d/Δ E_M increases linearly with the logarithm of d/Δ. This is shown in panel **b**. The error in shock time-of-arrival, ΔT, shown in panel **b**, decreases smoothly with increasing d/Δ as long as $d/\Delta \geq 10$, while for

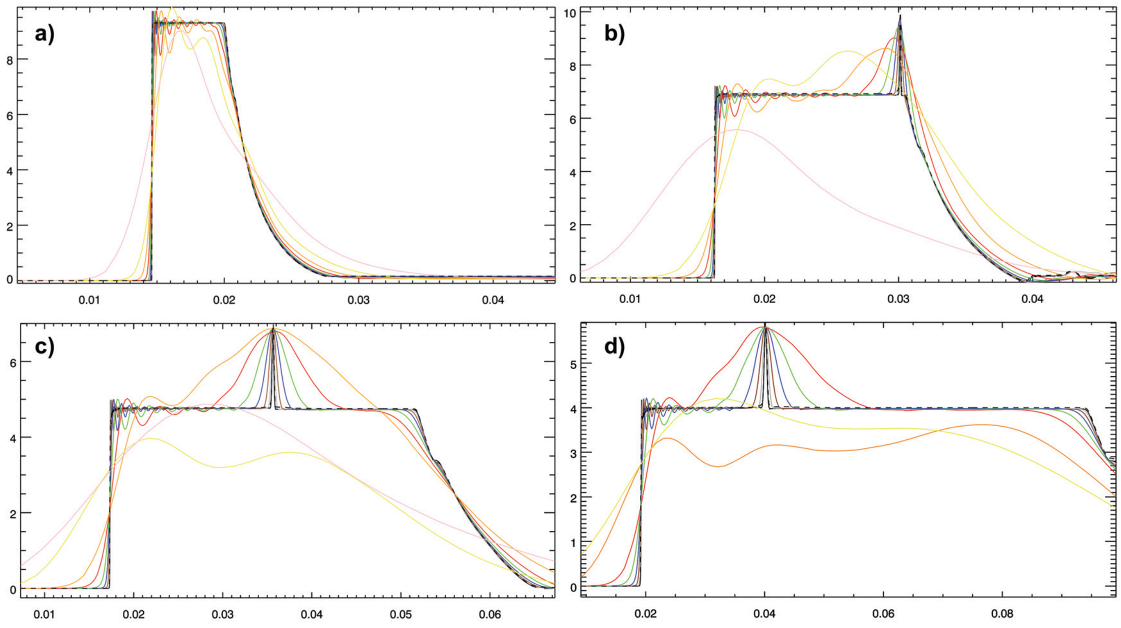

*Figure 3.4 Recorded pressure profiles (in units of GPa) as functions of time (in units of µs). The virtual measurements are taken 0.02 mm from the impact surface, into the pellet (sensor 1). The simulated flyer thickness is 25 µm (***a***), 50 µm (***b***), 100 µm (***c***), and 200 µm (***d***). The ratio of flyer thickness (d) to particle size (Δ) is 5 (pink), 10 (yellow), 20 (orange), 40 (red), 80 (green), 160 (blue), 320 (brown), 640 (grey), and 1280 (black). The black, dashed curves indicate the filtered, high resolution reference solutions.*

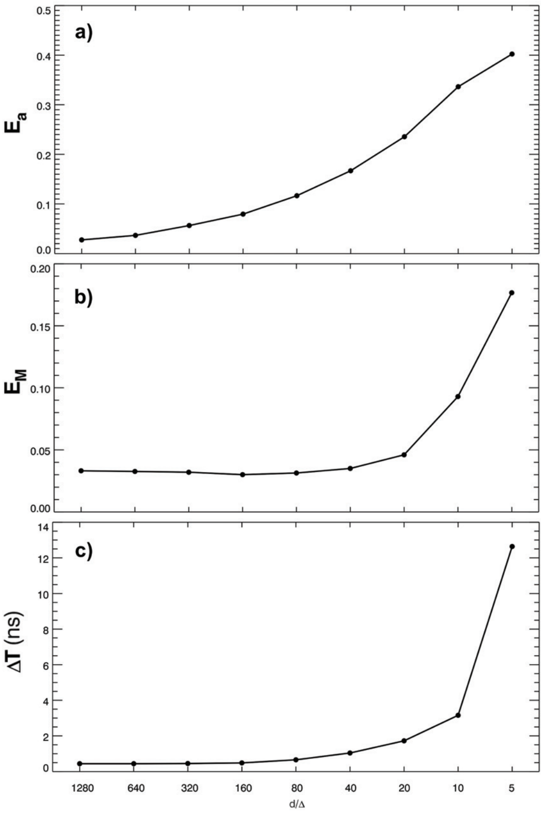

Figure 3.5 Sensor averaged error indicators, E_a (panel **a***), E_M (panel* **b***) and ΔT (panel* **c***) for the $d = 50$ μm as functions of the flyer thickness-to-particle size ratio (Δ/d).*

$d/\Delta = 5$, the shock is clearly under-resolved and results in a much increased δT. The reason for this sharp increase in ΔT can be that the algorithm used to determine the arrival of the shock fails to analyse the signal correctly when the shock has become too smeared out by the low resolution.

Finally, we combine the 3 error functions using Eq. 3.11 into the combined error function e_S. In Fig. 3.6 e_S is plotted as function of d/Δ for all 4 simulated values of flyer thickness. The black, brown, green and blue curves show the error function for $d = 25$ μm, $d = 50$ μm, $d = 100$ μm, and $d = 200$ μm, respectively. We see that the trend is qualitatively similar for all values of d, e_S decreases with increasing d/Δ. Still for $d/\Delta \geq 40$, the slope of the curves for $d = 25$ μm, and to some extent $d = 50$ μm, is very small compared to the slopes of the curves corresponding to the two thicker flyers. A comparison of the 3 error functions which e_S depends on shows that the two pressure-dependent error functions, E_a and E_M behave in much the same way when resolution is increased for all 4 flyer thickness values. It is ΔT, the shock time-of-arrival error, which is the main reason for the difference in the e_S trend in the medium-to-high resolution regime between thinner and thicker flyer results. The drop in ΔT levels off as one goes to higher-and-higher resolution. This occurs at a lower d/Δ-ratio when the flyer is thinner, indicating a small error which is not determined by resolution.

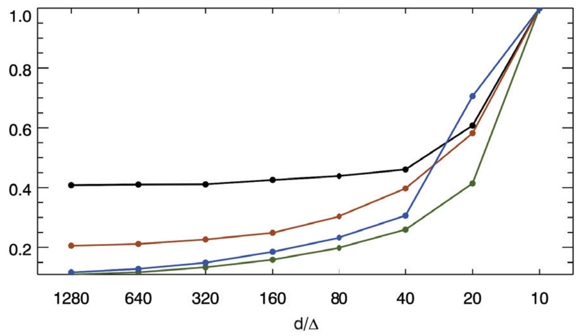

Figure 3.6 Combined error indicator, e_S*, for flyer thickness* $d = 25$ *µm (black),* $d = 50$ *µm (brown),* $d = 100$ *µm (green), and* $d = 200$ *µm (blue line) as function of the flyer thickness-to-particle size ratio (*Δ/d*).*

4 Implementing Ignition and Growth model in SPH

So far, we have only considered flyer impact on inert pellets. In order to simulate the corresponding process with explosive pellets, it must be determined how the I&G model defined in section 2.5 is best implemented in an SPH code. In the current work we restrict our focus to flyer-initiation of HNS-IV, so we cannot be certain a given I&G model implementation will work equally well for different explosive materials. The model parameters for HNS-IV listed in Table 2.2 were, at least in part, determined based on numerical results obtained with a completely different type of method than the currently used method (Tarver & Chidester, 2014). It is unclear whether this set of parameter values will reproduce the best fit to experimental data when using an SPH method. Still, the parameter values of Table 2.2 is used as a starting point when trying to determine a calibrated SPH model for flyer-induced ignition of HNS-IV.

Implementing an ignition model within the framework of SPH should be relatively straightforward, and there exist a few papers discussing the use of such models in SPH codes (Wang et al., 2015; Yang et al., 2013). However, none of them uses the model in the context of flyer impact initiation. It is therefore an open question what would be the best SPH implementation of the I&G model for the current application. In this section we compare the results obtained using a handful of slightly different algorithms.

4.1 Reference algorithm

The first algorithm applies the I&G model equations , Eqs. 2.51-2.54, directly to calculate the burn rate for each SPH particle using a standard predictor-corrector scheme. With this scheme the burn ratio, F_a of particle a at the half time step $t+\Delta t/2$ is first estimated using the burn rate at the old time step. Through the explosive EOS, an increase in the burn ratio also implies a corresponding increase in the pressure. With the predicted half-step values of F_a and P_a, in addition to the old value of the density ρ_a, a corrected estimate of the half-step burn rate, dF_a/dt, can be calculated. Finally, the burn ratio can be integrated in time from t to $t + \Delta t$. Once the burn ratio is updated, the thermal energy and pressure is updated in accordance with the explosive EOS. The reference algorithm uses the same time step for the burn integration as for the time integration of the hydrodynamic equations of motion.

4.2 Time integration using sub-steps

The burn rate equation is highly non-linear since it depends strongly on the burn rate, both directly, as given by Eqs. 2.51-2.54, as well as indirectly through the EOS. We therefore also consider using smaller time steps for the burn ratio integration. In this version of the algorithm, each HNS particle integrates the burn ratio from t to $t + \Delta t$ by applying a number of smaller time steps, referred to as sub-steps. The maximum number of sub-steps allowed is given by the global constant $N_{\text{sub,max}}$ and the minimum sub-step length, $\delta t^{\text{min}}_{a,s}$ where s is the sub-step index and a is the particle index, is defined as $\Delta t/N_{\text{sub,max}}$. The maximum allowed length of $\delta t_{a,s}$ is

$$\delta t^{\text{max}}_{a,s} = \Delta t - \sum_{k=0}^{s-1} \delta t_{a,k}. \tag{4.1}$$

Without considering the upper and lower limits, the length of a sub-step $\delta t_{a,s}$, is first estimated to be

$$\widehat{\delta t}_{a,s} = \frac{1}{N_{\text{sub,max}} dF_{a,s}/dt}, \tag{4.2}$$

where the burn rate $dF_{a,s}/dt$ is updated for each sub-step using the predictor-corrector scheme already described in section 4.1. Finally, the length of sub-step $\delta t_{a,s}$ is then given as

$$\delta t_{a,s} = \begin{cases} \delta t^{\text{min}}_{a,s} & \text{if } \widehat{\delta t}_{a,s} \leq \delta t^{\text{min}}_{a,s}; \\ \delta t^{\text{max}}_{a,s} & \text{if } \widehat{\delta t}_{a,s} \geq \delta t^{\text{max}}_{a,s}; \\ \widehat{\delta t}_{a,s} & \text{otherwise.} \end{cases} \tag{4.3}$$

In the current work, $N_{\text{sub,max}}$ has been set as high as 1000, but the number of sub-steps actually required by the HNS particles is seen to be much less. As an example, we look at the case of a 100 μm thick flyer with impact speed 1.7 km/s. The maximum number of sub-steps in this case fluctuates from between 5-6 and 50-60, and the average number of sub-steps used by the HNS particles is not more than roughly 1.2. The total CPU-time has increased by around 10%. The benefit from applying the sub-stepping is illustrated for this case in Fig. 4.1 where simulation results both without (panels **a** and **c**) and with (panels **b** and **d**) sub-stepping is shown. The resolution in both cases is given by $d/\Delta = 80$. The top panels show pressure profiles (in GPa) in a 0.25 μm interval, while the bottom panels show the corresponding profiles of the reaction ratio. We see that the solution without sub-stepping exhibits high-frequency noise which is more or less eliminated when sub-stepping is applied. The difference is particularly clear in the reaction ratio profiles.

4.3 Burn ratio smoothing

As an extra measure to reducing numerical noise in the burn ratio profile, we have also considered adding an additional smoothing procedure to the ignition algorithm. The idea is that the burn rate is calculated for each particle completely without considering the neighbouring particles, and that this lack of spatial communication might contribute to a more noisy burn ratio field. The spatial smoothing is performed on the burn ratio data right after updating the data according to the method described in section 4.2. The smoothing was initially performed on all HNS-particles according to the method described by Eq. 2.5, with the only exception that only neighbouring HNS-particles were included in the summations. The smooth burn ratio would then replace the unfiltered value under the condition that the smooth ratio cannot decrease from one time step to the next. Although the smoothing procedure could possibly be beneficial when simulating thick flyers, the procedure was shown to put unphysical restrictions on the ignition process for thinner flyers. It was therefore decided to use the sub-stepped burn ratio time integration without any additional spatial smoothing.

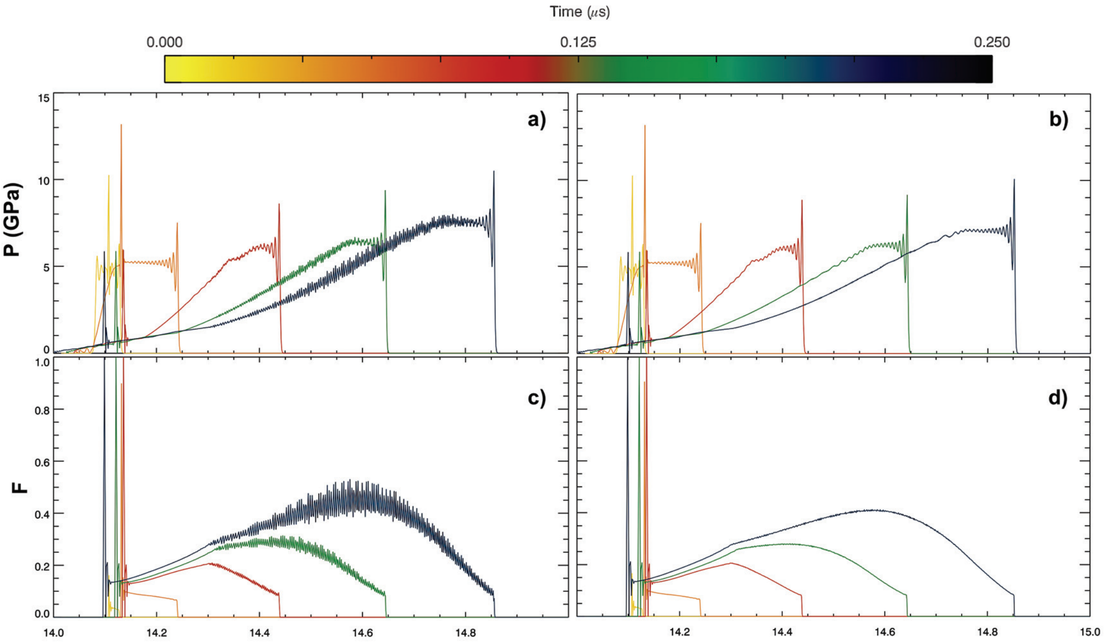

Figure 4.1 *Simulation results of a d =* $100\mu m$ *flyer impacting an HNS pellet with velocity 1.7 km/s. Results are shown both without (panels* **a** *and* **c***) and with (panels* **b** *and* **d***) sub-step integration of the I&G equation. The top panels show pressure profiles (in GPa), while the bottom panels show profiles of the reaction ratio. The colour indicates at which point in time each profile is taken.*

5 One-dimensional simulations of flyer impact on reactive HNS pellets

In this section we investigate the accuracy of the I&G model for flyer impact on reactive HNS-IV. In particular, we are interested in looking at numerical convergence and the possible need for adjusting the I&G model parameters for HNS-IV relative to what is listed in Table 2.2. All simulations in this section are performed in one dimension and therefore assumes flyers and pellets with infinitely large cross-sections. The primary parameter in addition to the flyer diameter, is the impact velocity. A moderate flyer velocity might be sufficient to cause a partial ignition response, without igniting the whole pellet. However, once the velocity is increased above a critical threshold value, an unstable ignition process is started. As one might expect, there is some spread in the empirical data found in literature on the critical flyer velocity, v_f, for detonation of HNS-IV as a function of flyer material, thickness, and diameter (Bowden, 2018; Bowden et al., 2012; Damm & Dudley, 2010; Kipp & Setchell, 1988). To simplify comparisons, we use the empirical data for infinite diameter Kapton flyers provided in (Tarver & Chidester, 2014), and which are listed in Table 5.1, as reference results.

The outcome of ignition simulations naturally separates into two well defined categories. Either the reaction ratio never reaches unity which means that the explosives never detonate, or detonation occurs after the shock wave has propagated a certain run distance. The difference in the solutions with or without ignition is best illustrated by looking at an example. Here, we take a close look at the case with flyer thickness 50 μm. The critical velocity according to Table 5.1 for this case is 2.2 km/s for impact on HNS-IV. We simulate the impact process for two cases of flyer velocity, 2.1 km/s and 2.2 km/s, with a high-resolution representation ($d/\Delta = 640$). Fig. 5.1 shows results from the lower velocity case in panels **a** and **c** and the higher velocity case in panels **b** and **d**. The top panels show pressure profiles (in GPa), while the bottom panels show profiles of the reaction ratio. Again, the colour indicates the time at which each profile is taken. Although the initial conditions are almost identical in the two cases, with only 0.1 km/s difference in initial flyer velocity separating them, the end result in the two cases is widely different. Up to about 0.2 μs, the two solutions are very similar. However, as the reaction ratio only reaches a critical level in the higher velocity case, the two solutions soon diverge. Flyer velocity 2.1 km/s results in a quasi-steady shock front where the pressure drops slowly and the simulation is stopped after a pre-determined time period of 0.8 μs. In contrast, full ignition is achieved in less than 0.4 μs when the flyer velocity is increased to 2.2 km/s. The run-to-detonation distance is about 1 μm. Note also the characteristic delay of the pressure peak relative to the shock front location when full ignition is achieved.

To more easily be able to quantify the difference in outcome between different simulations, we

Table 5.1 Critical flyer velocity for a Kapton®flyer impacting an HNS-IV pellet as function of flyer thickness d.

d (in μm)	12.5	25	50	100	200
v_f (in km/s)	3.0	2.7	2.2	1.7	1.5

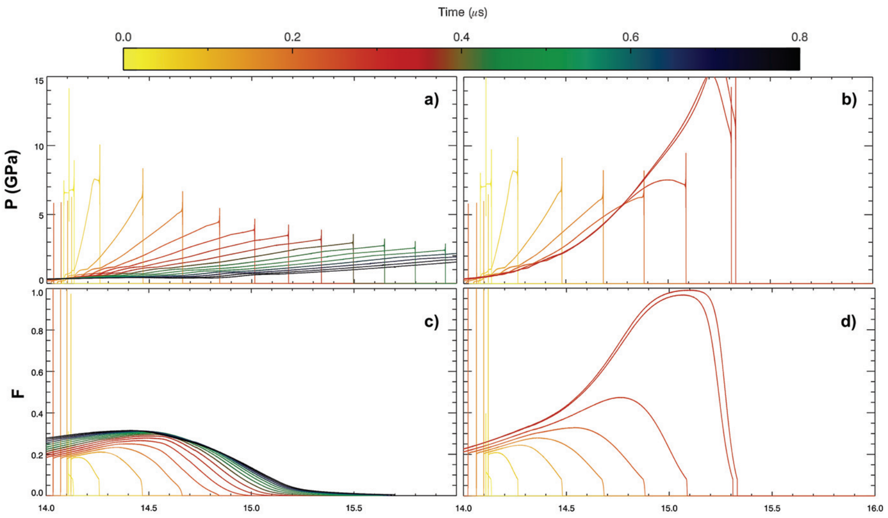

Figure 5.1 *Simulation results of a $d = 50$ μm flyer impacting an HNS pellet. Results are shown for flyer velocity 2.1 km/s (panels* **a** *and* **c***) and 2.2 km/s (panels* **b** *and* **d***). The top panels show pressure profiles (in GPa), while the bottom panels show profiles of the reaction ratio. The colour indicates at which point in time each profile is taken.*

define a scalar quantity which we call the **ignition indicator**, denoted f_d, as:

$$f_d = \begin{cases} \mathrm{Max}(F) - 1 & \text{if } 0 \leq F < 1; \\ \frac{L_0}{L_{\mathrm{run}}} & \text{otherwise,} \end{cases} \tag{5.1}$$

where $\mathrm{Max}(F)$ is the maximum reaction ratio at the end of the simulation, L_{run} is the run distance to detonation, and $L_0 = 1$ mm is a reference length. With this definition, $f_d < 0$ when detonation is not reached. For cases where the flyer velocity is just slightly larger than the critical velocity, f_d is positive but is expected to be fairly small since L_{run} should be relatively large. In practise, we see that L_{run} rarely is above 1-2 mm so that f_d will typically exhibit a jump as the flyer velocity is gradually increased above the critical velocity.

5.1 Resolution requirement for simulations of flyer impact on reactive HNS-IV

In section 3.2 we looked at convergence in the case of flyer impact on inert HNS. Here, we investigate how the outcome a flyer-induced ignition process in reactive HNS-IV changes with changing resolution. As before, we assume a uniform and constant smoothing length, h, with the particle spacing initially being 1.5 times smaller than h. The resolution is given by the ratio of the flyer thickness d to the particle spacing Δ, and simulations have been performed with d/Δ ranging from 10 to 640. First, we focus on the three cases $d = 50$ μm, $d = 100$ μm, and $d = 200$ μm, and in each case the impact velocity is varied from -0.4 km/s to +0.3 km/s relative to the critical flyer velocity listed in Table 5.1 with an increment of 0.1 km/s.

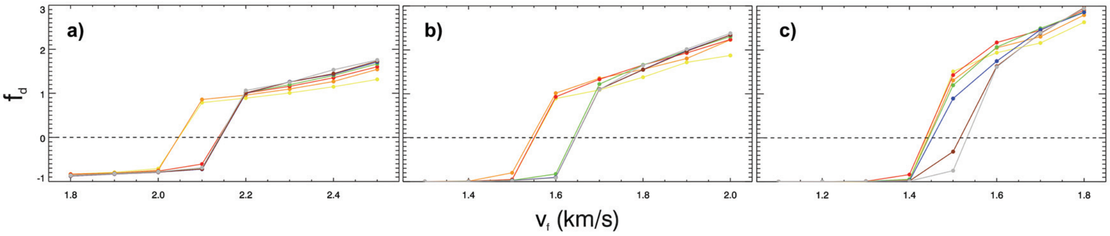

Figure 5.2 Ignition indicator, f_d, plotted as function of flyer impact velocity, v_f. Results are plotted for flyer thickness d equal to 50 μm (panel **a***), 100 μm (panel* **b***), and 200 μm (panel* **c***) and for resolution parameter d/Δ equal to 10 (yellow), 20 (orange), 40 (red), 80 (green), 160 (blue), 320 (brown) and 640 (grey).*

Fig. 5.2 summarises the results. Panels **a**, **b**, and **c** show the ignition indicator for d = 50μm, d = 100 μm, and d = 200 μm, respectively. The colour of each curve indicates the resolution where d/Δ equals 10 (yellow), 20 (orange), 40 (red), 80 (green), 160 (blue), 320 (brown) and 640 (grey). The ignition indicator increases with flyer velocity as expected, and we recognise the step in f_d where the solution goes from partial reaction to full ignition. In all three cases, the difference between the numerically obtained critical velocity and the tabulated values are within 0.1 km/s, the same as the resolution of simulated flyer velocity. The variation in critical velocity with changing resolution is also within 0.1 km/s, with the coarser solutions tending to be slightly more sensitive than the finer solutions. This is probably due to larger pressure fluctuations seen when the resolution is lower.

The maximum value of f_d for the simulated velocity range increases, and converges, with increasing resolution, for all three flyer thickness values. For d = 50 μm the maximum value of f_d is about 25% lower for d/Δ = 10 compared to the d/Δ = 640 result. For d/Δ = 20 this difference is reduced roughly by a factor 2. For d = 100 μm, this low-resolution error is reduced slightly and for d = 200 μm it is roughly half of that found in the d = 50 μm case. A resolution of d/Δ = 20 should therefore be an acceptable compromise between accuracy and CPU efficiency, at least for flyer thickness around 50 μm or more.

5.2 Modification of the HNS-IV I&G model for flyer thickness below 50 μm

The ignition model parameter $F_{0,\max}$ sets the upper reaction ratio limit to the first reaction rate term in Eq. 2.51, dF_0/dt. The default HNS-IV value for this parameter is 0.08. However, it is pointed out in Tarver & Chidester (2014) that for flyers thinner than 20 μm, a higher reaction ratio during the first shock compression phase is needed for the proper threshold velocity to be modelled. A similar increase in $F_{0,\max}$ has been shown to be needed for successful modelling of especially short pulsed initiation of other explosives in 1D and for 2D with small diameter (May & Tarver, 2009; Tarver & May, 2010). In Tarver & Chidester (2014), $F_{0,\max}$ is increased from 0.08 to 0.18 when the flyer thickness is reduced below 20 μm. The discrete nature and magnitude of the parameter change calls for additional investigations into this particular part of the model. It seems natural that in reality, $F_{0,\max}$ should see a more gradually increase as the flyer thickness is reduced. The idea that the parameter change described in Tarver & Chidester (2014) is only a coarse representation of a more smooth behaviour of $F_{0,\max}$, is strengthened by the fact that the numerically obtained

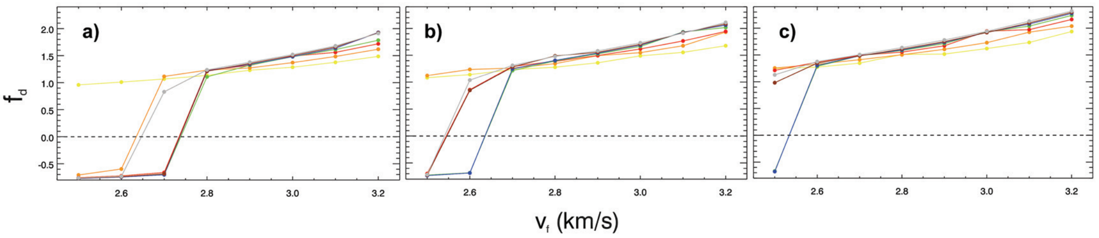

Figure 5.3 *Ignition indicator, f_d, plotted as function of flyer impact velocity, v_f for flyer thickness $d = 25$ μm. Three, slightly different, I&G models are considered where the parameter $F_{0,max}$ is set to 0.12 (panel **a**), 0.13 (panel **b**), and 0.14 (panel **c**). Results are shown for resolution d/Δ equal to 10 (yellow), 20 (orange), 40 (red), 80 (green), 160 (blue), 320 (brown) and 640 (grey).*

critical flyer velocity in Tarver & Chidester (2014) for flyer thickness 25 μm is about the same as that obtained for 10 μm, roughly 3.1 km/s. The experimental data, on the other hand, indicate a strong critical velocity dependence on flyer thickness when the flyer thickness is less than 50 μm.

5.2.1 $F_{0,\max}$ for the case $d = 25$ μm

First, the current work shows that the modelling of shock-initiated ignition due to the impact of thin flyers is highly sensitive to the numerical model used, in particular the resolution and the level of numerical dissipation. Since the required resolution is related to the thickness of the flyer, it will be increasingly demanding to get an adequate representation of the problem when the flyer thickness is reduced. Secondly, our results indicate that a moderate increase in the parameter $F_{0,\max}$ is needed already when the flyer thickness is as small as 25 μm. In Fig. 5.3, the ignition indicator is plotted as function of flyer velocity for $F_{0,\max} = 0.12$ (panel **a**), $F_{0,\max} = 0.13$ (panel **b**), and $F_{0,\max} = 0.14$ (panel **c**). By comparing the three models, we see the effects that small changes to $F_{0,\max}$ have on the outcome. Results are shown for resolution d/Δ equal to 10 (yellow), 20 (orange), 40 (red), 80 (green), 160 (blue), 320 (brown) and 640 (grey). According to Table 5.1, the critical velocity for this flyer thickness should be approximately 2.7 km/s, and simulations have been performed in the interval from 2.5 km/s to 3.2 km/s.

Choosing $F_{0,\max} = 0.14$ clearly results in the HNS being too sensitive, with only the $d/\Delta = 80$ and $d/\Delta = 160$ solutions giving a threshold velocity close to the experimental result. When the resolution is maximised, the best fit to the experimental value is obtained with $F_{0,\max} = 0.12$. The numerically obtained critical velocity is exactly 2.7 km/s and the value of the ignition indicator increases from roughly 0.8 at flyer velocity 2.7 km/s to around 1.9 at 3.2 km/s. However, it is unrealistic to be able to run two- and three-dimensional simulations with d/Δ as high as 640. Choosing $F_{0,\max} = 0.13$ might give a more accurate result when one is forced to run the simulation with a more moderate resolution. If we look at the red curve in panel **b**, we see that the $d/\Delta = 40$ solution in this model has a critical velocity of 2.6 km/s with $f_d = 0.8$. At flyer velocity 3.2 km/s, the value of the ignition indicator is almost identical in $d/\Delta = 40$ as it is for the maximum resolution solution in model **a**. We therefore choose to use $F_{0,\max} = 0.13$ for flyer thickness 25 μm as standard.

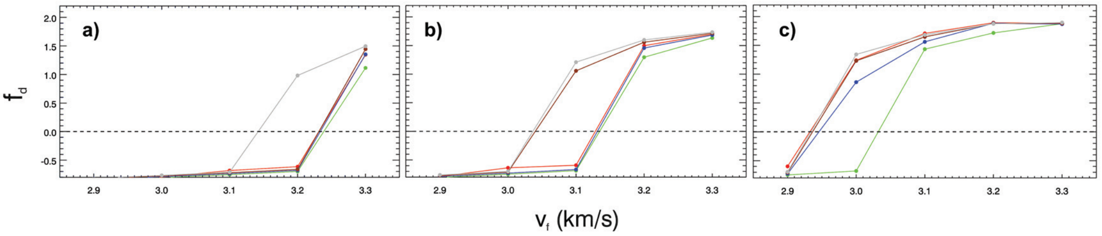

*Figure 5.4 Ignition indicator, f_d, plotted as function of flyer impact velocity, v_f for flyer thickness d = 12.5 μm. Three, slightly different, I&G models are considered where the parameter $F_{0,max}$ is set to 0.19 (panel **a**), 0.20 (panel **b**), and 0.21 (panel **c**). Results are shown for resolution d/Δ equal to 40 (red), 80 (green), 160 (blue), 320 (brown) and 640 (grey).*

5.2.2 $F_{0,\max}$ for the case $d = 12.5$ μm

In this work, we are interested in flyer thickness as small as about 10 μm. If we assume that $F_{0,\max}$ should be increased as the flyer thickness is decreased, we must recalibrate $F_{0,\max}$ for the smallest relevant values of the flyer thickness. For this reason, we repeat the exercise in section 5.2.1, but this time for $d = 12.5$ μm. In order to keep the relative resolution, d/Δ, the same as in the previous case, we need to decrease the particle size (and the time step) by a factor 2. Relative to the $d = 100$ μm case, the resolution requirement is increased by almost a factor 10. This gives a small indication of how much more challenging it is to simulate a flyer when the thickness is $d = 12.5$ μm rather than $d = 100$μm. However, since the simulations so far are performed in 1D, we are able to maintain the same high relative resolution, even for the thinnest flyers.

For $d = 12.5$ μm, the experimental estimate of the critical flyer velocity in a 1D case is 3.0 km/s. In Fig. 5.4, we see the numerical results for the three models distinguished by $F_{0,\max} = 0.19$ (panel **a**), $F_{0,\max} = 0.20$ (panel **b**), and $F_{0,\max} = 0.21$ (panel **c**). Again we can see how the sensitivity of the HNS is increased when $F_{0,\max}$ is increased. Results are this time shown for relative resolution, d/Δ, equal to 40 (red), 80 (green), 160 (blue), 320 (brown) and 640 (grey). Flyer velocities in the range 2.9 km/s to 3.3 km/s are modelled. Model **a**, corresponding to the smallest value of $F_{0,\max}$, clearly renders the explosives too insensitive. The same applies to some extent to model **b**, while model **c**, with $F_{0,\max} = 0.21$, gives a reasonably good fit, even when the resolution is moderate. If $F_{0,\max}$ is increased to 0.22 (not shown in Fig. 5.4), the HNS in contrast becomes too sensitive. We therefore choose $F_{0,\max} = 0.21$ for flyer thickness 12.5 μm.

Note that this is slightly higher than the value 0.18 suggested for thin flyers in Tarver & Chidester (2014). Fig. 5.5 shows the simulated pressure (panel **a**) and reaction ratio (panel **b**) for the $d = 12.5$ μm flyer with initial flyer velocity 3.1 km/s. when $F_{0,\max} = 0.20$ and $d/\Delta = 640$, while Fig. 5.6 shows the corresponding plots for $F_{0,\max} = 0.21$. Notice how the small change in $F_{0,\max}$ has a considerable impact on the ignition process. Despite the fact that the two solutions have very similar pressure profiles for the first 50-100 ns after impact, the run-to-distance distance is about 25% shorter when $F_{0,\max}$ is increased from 0.20 to 0.21. The time-to-detonation is correspondingly reduced by as much as 50 %. Given that the flyer velocity in this case is just above the expected critical velocity, the $F_{0,\max} = 0.20$-solution is likely to be slightly more correct than the $F_{0,\max} = 0.21$-solution in this high-resolution case. Considering the fact that a lower resolution level most likely must be chosen in multi-dimensional simulations, we still choose to use $F_{0,\max} = 0.21$ as the default setting.

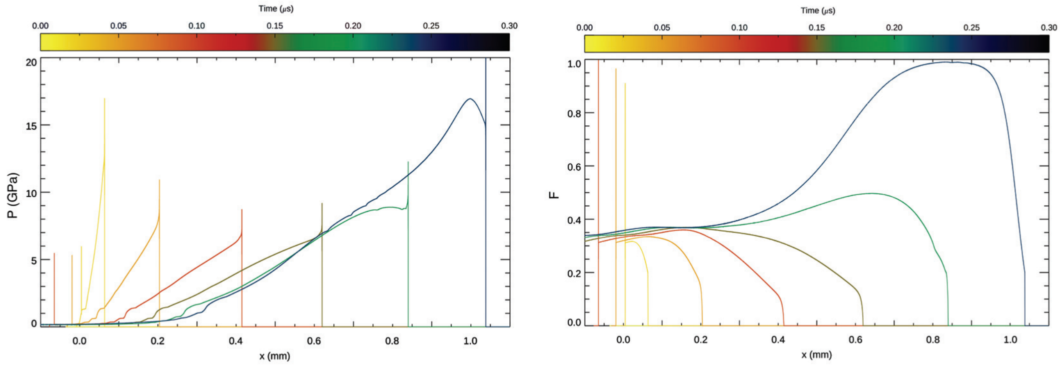

Figure 5.5 *Simulation results of a d* = 12.5 *μm flyer impacting an HNS pellet. Results are shown for flyer velocity 3.1 km/s using* $F_{0,max}$ = 0.20 *and* d/Δ = 640. *Panel* **a** *shows pressure profiles (in GPa), while panel* **b** *shows the corresponding profiles of the reaction ratio. The colour indicates at which point in time each profile is taken.*

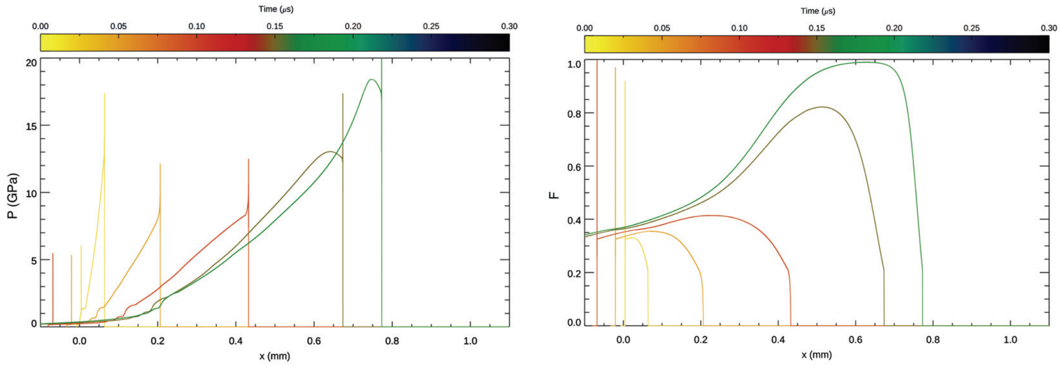

Figure 5.6 *Simulation results of a d* = 12.5 *μm flyer impacting an HNS pellet. Results are shown for flyer velocity 3.1 km/s using* $F_{0,max}$ = 0.21 *and* d/Δ = 640. *Panel* **a** *shows pressure profiles (in GPa), while panel* **b** *shows the corresponding profiles of the reaction ratio. The colour indicates at which point in time each profile is taken.*

6 Simulating thin flyer impact on explosive pellets in 2D and 3D

Now we turn our attention to the simulation of flyer impact on HNS-IV pellets in 2D and 3D. As a rule of thumb estimate, increasing the resolution in 1D by a factor of 2 gives roughly a factor of 4 increase in computing time. In 2D and 3D, the corresponding increase is 8 and 16, respectively. In other words, increasing the resolution is much more CPU demanding in 3D (and 2D) than in 1D. REGULUS has so far not been prepared for parallel computing, either on multi-core CPUs or on GPUs. Given the strict resolution requirements determined in section 5.1 for this class of applications, we are completely dependent on utilising other features in the code which help to reduce the CPU load in multidimensional simulations. We will therefore discuss three solver options that are available in REGULUS and which could potentially be applied in order to limit the CPU load. These options are: using variable resolution using particle regularization, utilising a variable computational domain using inflow and outflow, and replacing the Cartesian formulation in 2D and 3D with a cylindrical formulation in 1D and 2D. Although the main focus here is on numerical issues associated with the simulations of thin flyer ignition of HNS pellets in 2D and 3D, this chapter will also include a brief discussion of the effect of finite flyer width in a 2D setup for 75 μm thick flyers.

6.1 Simulations of flyer-induced ignition using variable resolution

Traditionally, SPH has been used with equal-mass particles (within the same material) so that the mass density is strictly proportional to the particle number density. To improve accuracy and efficiency, the smoothing length should vary according to the local particle spacing, which implies a varying resolution both in time and space. Unfortunately, using equal-mass particles can in certain cases be impractical. When simulating a compressible gas with a highly inhomogeneous initial density profile, equal-mass particles means much more computational effort is spent on high density regions than on low-density regions. Another example where a traditional SPH approach to variable resolution is sub-optimal is in the modelling of shock waves. These waves travel by definition faster than the particles with typically much higher density upstream than downstream of the shock front. Unless resolution in some way can be decoupled from the mass density, the resolution just in front of the shock will be insufficient relative to the resolution upstream.

REGULUS is based on a special version of SPH known as Regularized SPH (RSPH). RSPH offers more flexibility with regards to how computational resources are distributed, both spatially and temporally, and has been shown to provide good results on a range of shock dominated applications (Børve et al., 2006, 2001). It utilises a method of particle regularization where the numerical solution is automatically mapped from one discrete representation to the next at specified time step intervals. The main benefits of this approach is twofold. First, it can be used to maintain high resolution near features propagating relative to the fluid flow, such as shock fronts, even when such features are not sufficiently reflected in the mass density profile. Secondly, the aim is to limit the amount of particle disorder. This is because particle disorder could otherwise lead to numerical instabilities, or at least a reduction in achieved accuracy. However, these features come at a cost as variable particle mass and variable smoothing length is both associated with a certain error level. In addition, performing particle regularization also leads to additional numerical dissipation. For the

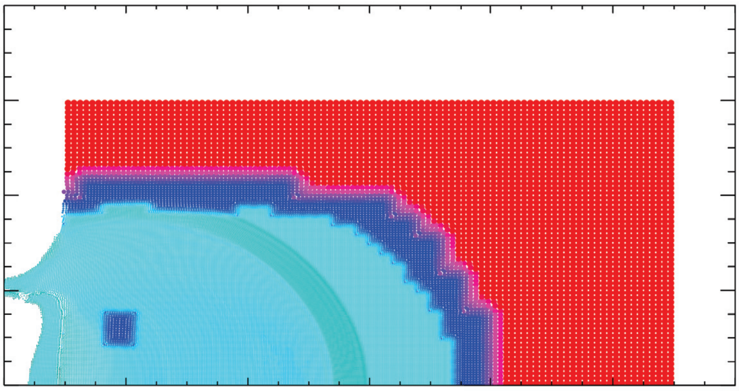

Figure 6.1 Colour map indicating the smoothing length in a 2D simulation of a 75 μm thick and 200 μm wide flyer impacting an HNS pellet with an impact speed of 3.8 km/s. The resolution ranges from about 0.002 μm (dark turquoise) to 0.015 μm (red).

current application, this means that the time period between consecutive executions of the particle regularization operation must be sufficiently long so as to avoid numerical dissipation levels high enough to affect the outcome of the ignition model.

6.1.1 Effect of particle regularization and variable resolution on I&G simulations

In this section we will investigate the effects of using particle regularization and/or variable smoothing length in simulations of flyer-induced ignition, and we will do this by looking at a specific example in 2D. A 75 μm thick and 200 μm wide flyer impacting an HNS pellet with an impact speed of 3.8 km/s. The size of the pellet is restricted to being 1000 μm long and 1200 μm wide. To speed up the numerical analysis, symmetry is assumed and only half of the full domain is simulated. The total simulation time is 0.2 μs. In all, 4 different simulations are performed.

The reference solution (solution **a**) uses equal-mass particles with an initial particle spacing of 2.5 μm and no regularization. The smoothing length varies in accordance with the fluid flow. This corresponds to a standard SPH solution. Solution **b** uses particle regularization at intervals of 200 time steps, where the particle distribution is returned to its original, uniform state. Unequal-mass particles in the initial distribution is introduced in solution **c**, while particle regularization is turned off. With no particle regularization, the initial smoothing length profile is chosen to only vary normal to the impact velocity, with the minimum value chosen in a zone twice the width of the flyer. Outside this high-resolution zone, the smoothing length increases to 4 times its minimum value.

The last solution included in this comparison, solution **d**, applies both particle regularization and variable resolution. During regularization, resolution is automatically optimised to ensure maximum resolution in regions where shock fronts are located. Solutions **a** and **b** both have a particle number of around 100.000. Solution **d** is the only solution where the particle number changes significantly, from roughly 15.000 to a final particle count of almost 100.000, with a time-averaged particle number of about half the final particle count. In comparison, solution **c** has a particle number of less than 40.000. Fig. 6.1 shows a map of the smoothing length profile in solution **d** at time $t = 0.1$ μs. The resolution ranges from about 0.002 μm, indicated by the darkest shades of turquoise, to a maximum of 0.015 μm in the red coloured outer region.

The 4 solutions are compared directly in Figs. 6.2 and 6.3. The first figure compares pressure fields at time $t = 0.1$ μs, with the colours reflecting the pressure level ranging from 0 (black) to 10 GPa or more (yellow). The second figure shows the burn ratio at time $t = 0.2$ μs, from 0 (black) to 1 (red). All solutions exhibit roughly the same shock front location and flyer shape. In the reference solution (solution **a**), there are pressure oscillations in the high pressure region behind the shock front, as one could expect. These oscillations are to a large extent reproduced in the 3 other solutions. Further upstream, the pressure field in the reference solution is relatively smooth. The same can be said about the entire burn ratio field in Fig. 6.3a where there is a smooth transition from the central, high burn ratio core region to the outer regions where very little or no ignition has taken place.

The difference between solution **a** and solution **b** is not so evident when comparing the $t = 0.1$ μs pressure profiles, although some extra oscillations are observed in the upstream, low-to-medium pressure regions. However, when comparing the $t = 0.2$ μs burn ratio fields of the two solutions, there is a distinct difference which could have a significant effect on the ignition outcome. The particle regularization used in solution **b** has created fairly strong, spherical disturbances in the burn ratio field. Since the burn ratio is a time-integrated quantity, it accumulates the disturbances generated by all calls to the regularization procedure. In fact, one can identify 5-6 sectors of almost identical thickness separated by the strong disturbances, each of which can be associated with a specific call to the regularization routine. The location of these strong disturbances is found to match the position of the shock front during the corresponding regularization process when we take into account the subsequent advection due to the fluid flow. During regularization, the mass of the particles in the new particle distribution is calculated as a function of both the new and old particle distributions and the mass density. Since the shock compresses the material it propagates through, the particle mass will increase upstream at the precise location of the shock front during regularization. This inhomogeneity in the particle mass will in turn lead to disturbances in the burn ratio.

Solution **c** explores the possibility of designing a smoothing length field using unequal-mass particles where the resolution is highest in a zone closest to the horizontal axis. In contrast, particle regularization is not employed in this solution. We see from Fig. 6.2 that the shock front is broadened where the shock waves has propagated into the region of lower resolution, as one could expect. There is however no signs of the additional, upstream disturbances as seen in solution **b**. The $t = 0.2$ μs burn ratio field of panel 6.3c is therefore almost identical to that of the reference solution if we restrict ourselves to the maximum resolution region. There are however disturbances in the transition zone where the smoothing length increases, which are clearly an artefact caused by the particle mass inhomogeneities. Finally, solution **d** has the most variation in particle mass since it varies both in time and space. This is therefore the solution of the four which exhibits the largest disturbances in the burn ratio. This indicates that using RSPH techniques which involve using unequal-mass particles, might not yield the best result for this particular application given the sensitivity of the I&G model.

6.2 Simulations of flyer-induced ignition using variable domain

One of the benefits of SPH as a computational method is the simplicity with which free surfaces can be handled. This implies that computations can easily be restricted to a smaller part of the domain filled with the material to be studied. As long as reflections from any artificial boundary do not reach regions of interest, the computational accuracy should not be significantly reduced. A

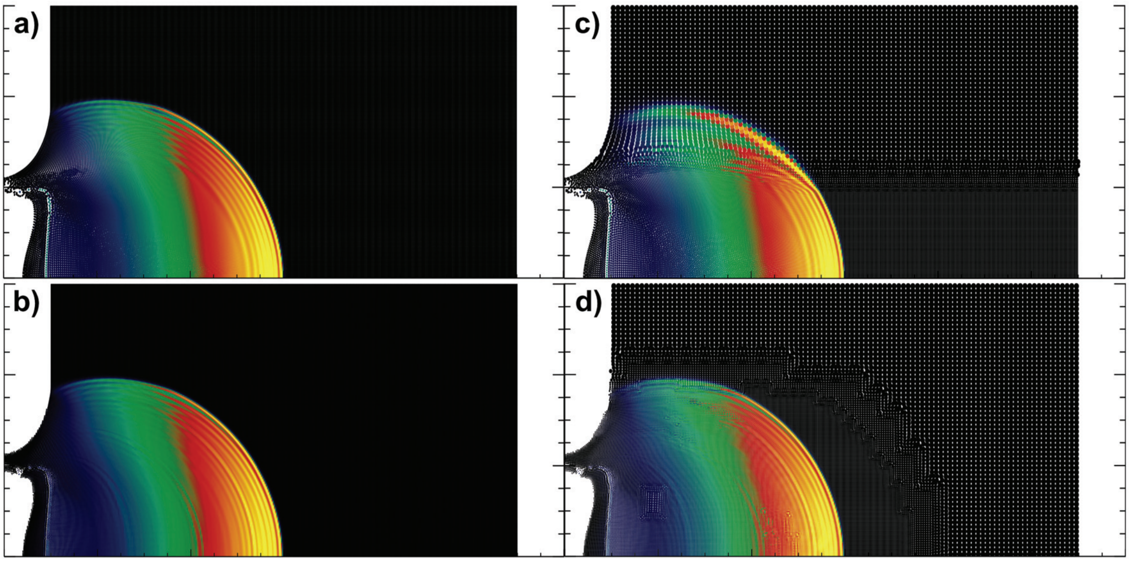

Figure 6.2 Pressure at time $t = 0.1$ μs in reference SPH solution (panel **a***), solution with uniformly distributed particle regularization (panel* **b***), solution with variable-mass particles without regularization (panel* **c***), and solution with resolution-optimised particle regularization (panel* **d***). The colours, from black to yellow, indicate pressure levels ranging from 0 to 10 GPa.*

challenge with the current application is that the shock front driving the ignition process propagates fast through the explosive material. If the run distance to detonation is sufficiently long, this requires an explosive pellet which is much longer and wider than the flyer that caused the shock wave in the first place. For instance, the flyer could have a thickness of 20 μm, while the pellet might have a diameter and length of more than 2000 μm. However, the most important physics to the ignition modelling occurs in a fairly small region behind the shock front, and because the shock front moves faster than any other signals in the application, this region of interest can effectively be isolated from regions further upstream. This type of problem can be solved more efficiently by applying inflow and outflow conditions on the boundaries perpendicular to the impact direction.

Once again, the numerical techniques are illustrated best by looking at a specific test problem. The flyer dimensions are the same as in the previous test, 75 μm thick and 200 μm wide. This time the flyer impacts with a speed of 3.7 km/s on a pellet which is 1.3 mm long and 2.0 mm wide. We will compare 3 solutions which all use equal-mass particles (corresponding to an initial particle spacing of 2.5 μm) with no particle regularization, where only the approach to inflow and outflow conditions vary. The first solution is once again a reference solution, with no inflow or outflow. The second solution uses inflow only, where new particles are continuously added downstream of the shock front, both at the right-hand vertical boundary and the top horizontal boundary. The rate at which particles are added along each inflow boundary is pre-defined and the location of the inflow boundaries propagate accordingly[4]. The inflow of particles along the vertical inflow boundary is stopped when the position of the boundary has reached the horizontal end position of the pellet.

---

[4] The appropriate speed of the inflow boundary could also be updated automatically by monitoring the propagation of the shock front. This would however require slightly more programming than the currently chosen option.

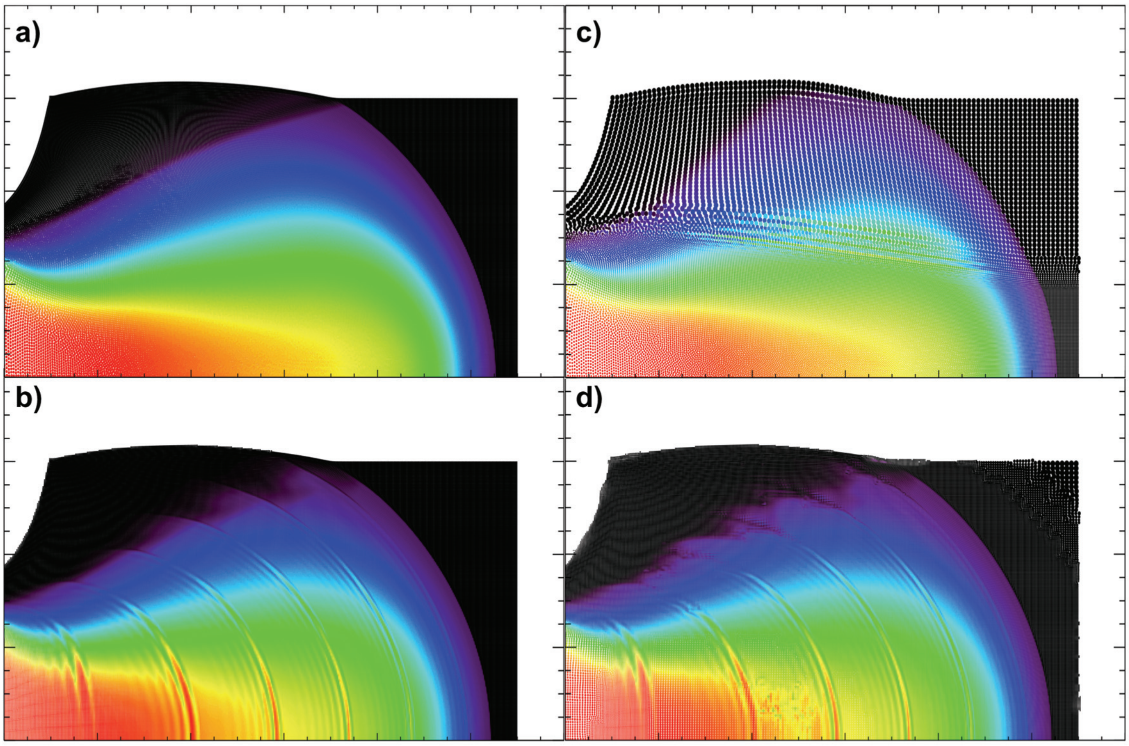

Figure 6.3 Burn ratio at time t = 0.2 *µs in reference SPH solution (panel* **a***), solution with uniformly distributed particle regularization (panel* **b***), solution with variable-mass particles without regularization (panel* **c***), and solution with resolution-optimised particle regularization (panel* **d***). The colours, from black to red, indicate burn ratios from 0 to 1.*

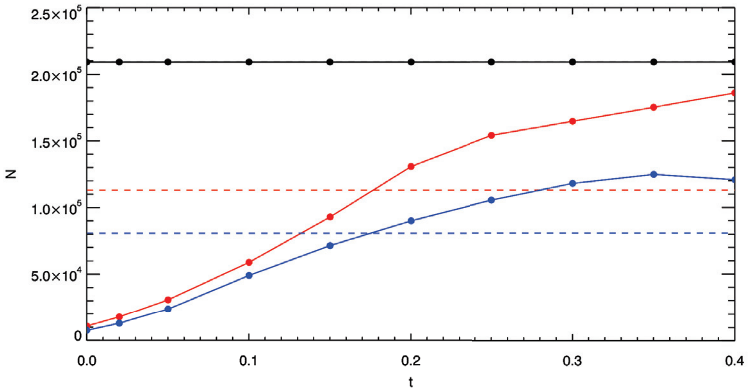

Figure 6.4 Particle number as a function of time in reference simulation (black curve), simulation with inflow only (red curves), and simulation with both inflow and outflow (blue curves). The dashed lines indicates the time-averaged particle number.

Inflow along the vertical inflow boundary is similarly restricted. In addition to the inflow procedure just described, the third solution also has outflow enabled along the left-hand, vertical boundary. The position of this outflow boundary is linked to the position of the inflow boundary by fixing the distance between them to 0.8 mm.

All 3 simulations assume the same initial particle spacing, but because of inflow (and outflow) the number of particles is constant only in the first simulation. Fig. 6.4 shows how the particle number varies in time up to the time $t = 0.4$ μs. In the reference simulation, the particle number is about 210.000, which is indicated by the black line in the plot. The total CPU-time in this simulation was almost one hour on a 2013 Mac Pro. Since the second simulation uses inflow but not outflow, the particle number will increase steadily until the entire pellet is included in the simulation domain. This is confirmed by the red, solid curve in Fig. 6.4 where we see that the particle number has increased from around 10.000 at the start of the simulation to almost 190.000 at $t = 0.4$ μs. The dashed, red line indicates a corresponding time-averaged particle number of just over 110.000, and the CPU-time is less than half that of the reference simulation. The inclusion of outflow ensures that the upper limit to the particle number is reduced by roughly 1/3 compared to the inflow-only solution. The time-averaged particle number is reduced by almost just as much although the initial particle distribution are the same. The CPU-time for the last simulation is only about 1/3 of what the reference simulation required.

No doubt, inflow and outflow makes simulations of flyer-induced ignition more efficient. The remaining question is whether this efficiency increase comes at the expense of reduced accuracy or not. Fig. 6.5 shows the pressure field at time $t = 0.2$ μs for the reference simulation (panel **a**) and the solution with both inflow and outflow (panel **b**). Fig. 6.6 shows the corresponding burn ratio fields at time $t = 0.4$ μs. It is apparent that although the second simulation has lost information about the flyer and the region of the pellet closest to the impact area, the two solutions show a great deal of similarities in most of the domain covered by both simulations. The errors caused by the inflow and outflow appear to be negligible. To investigate the differences between the three solutions in more detail, profiles along horizontal lines are plotted in Fig. 6.7. The top panel shows profiles of pressure at $t = 0.2$ μs while the bottom panel shows profiles of the burn ratio at time $t = 0.4$ μs. The profiles are taken at vertical distances 0.1 mm (black curves), 0.3 mm (green

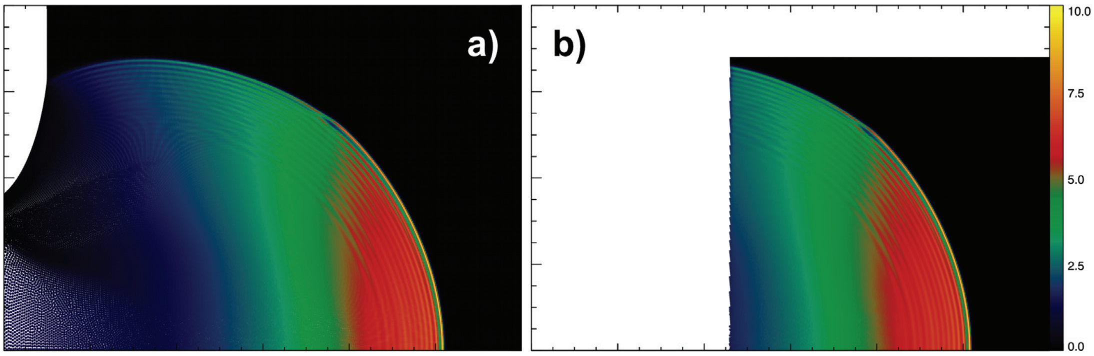

Figure 6.5 Pressure at time $t = 0.2$ μs in reference SPH solution (panel **a***) and solution obtained using inflow and outflow (panel* **b***). The colours, from black to yellow, indicate pressure levels ranging from 0 to 10 GPa.*

curves), and 0.5 mm (orange curves) from the horizontal axis. The solid curves show the reference solution, the dotted curves show the solution with only inflow, while the dashed curves show the solution with both inflow and outflow.

The pressure profiles confirm that the three solutions are very similar in the regions where they can be compared. There is slightly lower burn ratio levels in the two solutions using inflow or outflow, as seen in the bottom panel. This is probably because the burning rate depends heavily on the pressure and that the time-integrated burn ratio to some extent depends on the full upstream pressure profiles, which has been truncated in simulations with both inflow and outflow. There is a drop in pressure observed in simulation sufficiently far behind the shock front, despite not having used outflow in this case. The drop can be related to the fact that inflow is restricted to a 0.8 mm wide region upstream from the inflow boundary. By not imposing such a limit on the inflow, and also not allowing outflow, the burn ratio levels in the second solution will be more or less identical to that of the reference solution. Still, even the solution with both inflow and outflow exhibits only a modest error in burn ratio levels compared to the reference solution. The error is less than 2% 0.1 mm above the horizontal axis, while it is nearly 6% at the distance of 0.5 mm from the horizontal axis. In conclusion, using both inflow and outflow represents a valid compromise between accuracy and efficiency when simulating flyer-induced ignition.

6.3 Effect of flyer width W on the critical velocity for flyer thickness $d = 75$ μm

The effect of flyer diameter on ignition threshold velocity has been studied experimentally for the case of roughly 75 μm thick Kapton flyers impacting HNS-IV (Bowden, 2018) [5]. The pellet in this case had a diameter of 3.4 mm and a length of 1.3 mm. Threshold charge voltage and flyer velocity was defined as 50% probability of initiation. Two-dimensional simulations were performed at different impact speeds, with the flyer width W being equal to 200 μm, 300 μm and 600 μm. In addition, we have run one-dimensional simulations which correspond to infinite flyer width.

---

[5] It is noted that Kapton is highly ductile and that the flyer thickness at the point of impact is significantly smaller than the initial thickness. Impact flyer thickness of about 80% of its original value is indicated.

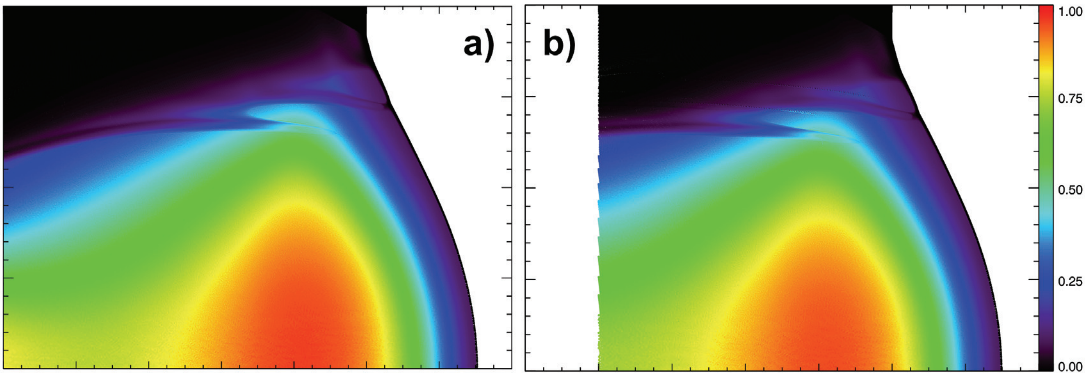

Figure 6.6 Burn ratio at time $t = 0.4$ µs in reference SPH solution (panel **a***) and solution obtained using inflow and outflow (panel* **b***). The colours, from black to red, indicate burn ratios from 0 to 1.*

Fig. 6.8 shows the pressure (left-hand panel), burn ratio (middle panel), and horizontal velocity (right-hand panel) at the time of ignition, $t = 0.25$ µs, for the case of flyer width 300 µm and impact speed 3.0 km/s. The initial particle spacing is 1.25 µm which implies a particle number which increases from around 40.000 initially to about 300.000 by the end of the simulation and a time-averaged particle number of 180.000. The plotted region is 600 µm by 670 µm.

Peak pressure is around 15 GPa. We see that the maximum pressure on horizontal lines is reduced by around 2 when the transverse distance from the symmetry line is about $2W$ (twice the original flyer width). The middle panel of Fig. 6.8 indicates that at the current initial flyer speed, full ignition at time $t = 0.25$ µs is roughly restricted to the original flyer width of $W = 300$ µm. At at distance of $2W$ from the symmetry line, the ignition ratio is only about 0.1. The last panel of 6.8 shows v_x, the fluid velocity in the original direction of flyer motion (horizontal component). The peak velocity is about 2.0 km/s, which is only 2/3 of the original flyer speed. At a distance of $1.5W$ from the symmetry line, the maximum horizontal velocity is reduced to half the value found at the symmetry line. At even higher vertical positions, the fluid flow is notably deflected so that the vertical velocity makes a dominating contribution to the speed. The maximum speed at a given vertical distance drops below 50% of the global maximum speed at around $2W$.

Fig. 6.9 shows critical flyer velocity ($v_{\mathrm{f,crit}}$) for the 75 µm thick flyer as a function of inverse flyer width W. The solid curves show the numerical results for the 2D plane symmetric case obtained with initial particle spacing equal to 1.25 µm (black curve) and 5.00 µm (grey curve). This corresponds to an initial ratio of flyer thickness to particle spacing of 60 and 15, respectively. In comparison, the dashed line shows the corresponding experimental results for the 3D setup (Bowden, 2018). The case where $1/W = 0\ \mathrm{mm}^{-1}$ corresponds to a 1D flyer geometry. In addition, flyer width values 200 µm, 300 µm, and 600 µm have been compared. First, we note that the numerical results is not as sensitive to resolution as one might expect, even though the coarsest resolution is slightly below the resolution requirement stated in 5.1.

For the 1D case and for $W = 600$ µm, the numerical results fit the experimental data fairly well. However, when the flyer width is reduced there is a noticeable difference between the experimental and numerical results which increases with decreasing flyer width. This is to be expected given the differences in the numerical and experimental setups. Since the simulated setup assumes an infinite

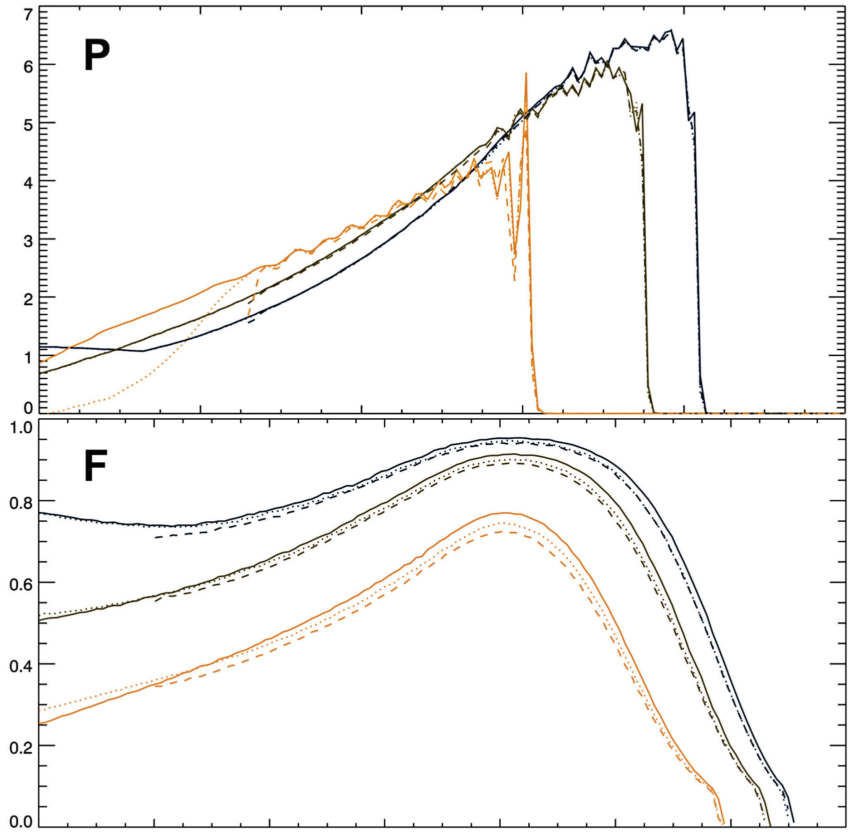

Figure 6.7 *Profiles of pressure at time $t = 0.2$ µs (top panel) and burn ratio at time $t = 0.4$ µs (bottom panel) as functions of the horizontal position. The profiles are taken at vertical distances 0.1 mm (black curves), 0.3 mm (green curves), and 0.5 mm (orange curves) from the horizontal axis. Three different solutions are compared: reference solution (solid curves), solution with inflow only (dotted curves) and solution with both inflow and outflow (dashed curves).*

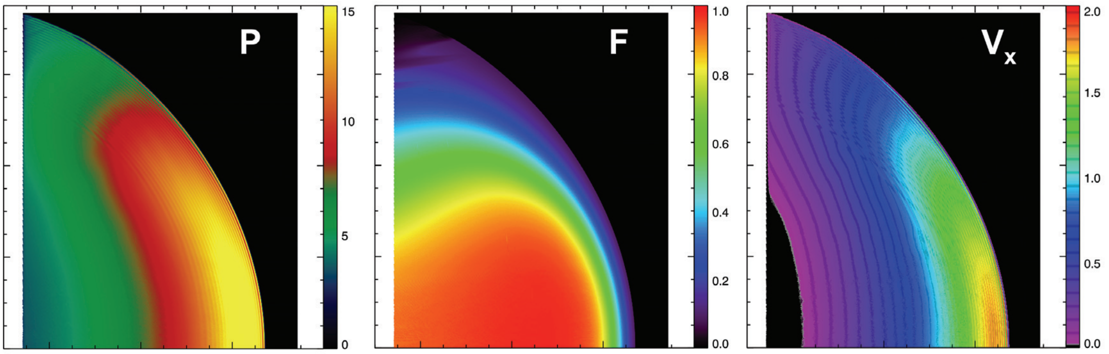

Figure 6.8 *Pressure in units of GPa (left-hand panel), burn ratio (middle panel), and horizontal fluid velocity in units of km/s (right-hand panel) at* $t = 0.25$ *µs, after the impact of a* $d = 75$ *µm thick and* $W = 300$ *µm wide flyer at a speed of 3.0 km/s. The target pellet has a length of 1.3 mm and a width of 3.4 mm. The distance between minor tick marks is 50 µm, In comparison, the initial particle spacing is 1.25 µm.*

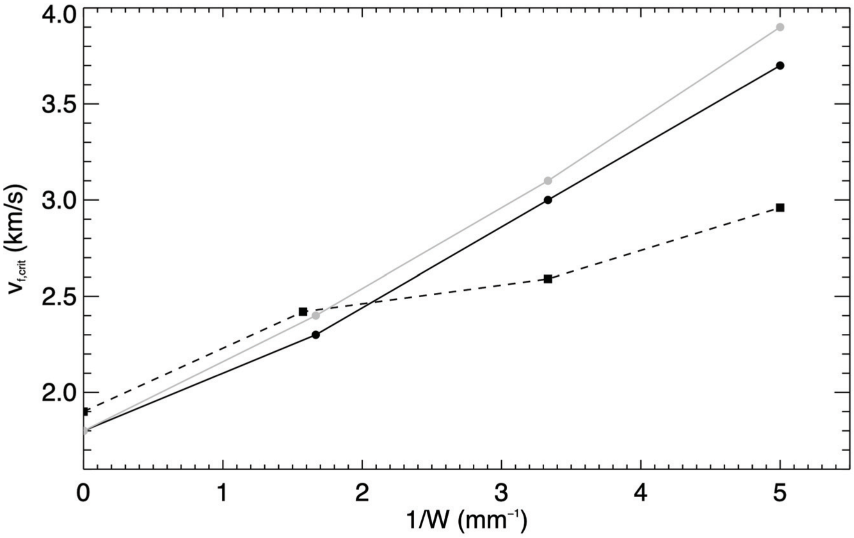

Figure 6.9 *Critical flyer velocity for a* $d = 75$ *µm thick flyer as a function of inverse flyer width W (in units of 1/mm). The solid curves represent numerical results obtained for a two-dimensional flyer with initial particle spacing equal to 1.25 µm (black curve) and 5.00 µm (grey curve). The dashed curve shows the experimental result for cylindrical flyers (Bowden, 2018).*

flyer height (as opposed to a finite flyer width) while the flyers in the experiments have roughly the same extension in both flyer plane directions, it is reasonable to expect that the difference between the numerical and experimental results increases with decreasing flyer width. However, one would expect the experimental results to exhibit a stronger rather than a weaker dependence on the flyer width compared to the numerical results. This prediction can be justified by the fact that the volume and surface area of a three-dimensional thin flyer depends on the flyer width squared, while the volume and surface area of a two-dimensional thin flyer depends linearly on the width. For the numerical results, $v_{\mathrm{f,\,crit}}$ is seen to increase almost linearly with the inverse flyer width, as expected. In the experimental case though, the increase in $v_{f\,,\mathrm{crit}}$ is particularly weak from $W = 600$ μm to $W = 300$ μm. Despite having cut the flyer width in half, the critical flyer velocity is only increased by a modest 6 %. In comparison, the corresponding increase in $v_{\mathrm{f,\,crit}}$ for flyer thickness 50 μm was in the experiments found to be more than 20 %, which is much closer to the numerical result of 30 % increase.

There is no guarantee the Kapton flyer in the experiments has maintained its original thickness and plane geometry during the flight phase, before impact. Additional simulations were performed with 200 μm wide, curved flyers where the radius of curvature was about 118 μm. The thickness and total mass of the curved flyers are the same as in the perfectly plane case. A comparison of the results from the curved and plane flyers shows that the critical flyer velocity increases slightly when the flyer is curved rather than plane. This is not at all that surprising since the convex shape of the curved flyer would produce a shock wave in the explosives which has a larger curvature than what is the case with a plane flyer. As a consequence, the pressure pulse is more easily dampened as the pulse propagates. Still, this effect could not account for the observed discrepancy between experimental and numerical results since the experimental flyers appear to be more effective than the plane, numerical flyers giving a lower critical velocity in the experiments.

6.4 3D simulation of flyer-induced ignition of HNS

Finally, we perform full 3D simulations of Kapton flyer impact in an HNS-IV pellet. Again we use the experiments in Bowden (2018) as a reference, and consider flyer thickness $d = 75$ μm, an initial flyer velocity of 2.5 km/s, and a pellet with a diameter of 3.4 mm and a length of 1.3 mm. In contrast to the experiments, we simulate rectangular flyers where the width is always the same in both directions perpendicular to the initial flyer velocity. Flyers with a width in the range 200-800 μm are considered. Based on the results in section 6.3, and considering the increased CPU cost when moving from 2D to 3D, we use a particle spacing of either 0.025 μm or 0.05 μm for the 3D simulations.

Unsurprisingly, we find that the 3D results are more sensitive to the flyer width than the corresponding 2D results. This implies that the difference between the numerical results and the experimental results indicated by the dashed curve in Fig. 6.9 becomes larger for low flyer width when switching the numerical model from 2D to 3D. Findings from 3D simulations with flyer width equal to 800 μm, 600 μm and 200 μm are summarised in Figs. 6.10, 6.11 and 6.12, respectively. All figures show snapshots taken at 0.05 μs (top row) and 0.09 μs (bottom row) after impact, and the panels show the density (panels **a** and **d**), the pressure (panels **b** and **e**), and the burn ratio (panels **c** and **f**). In each panel, the result for a flyer with infinite width, essentially the same as the 1D solution, is included (below the x-axis) for direct comparison. Coordinates in the figures are given in units of millimetre. Only one half of the flyer is simulated and symmetry along the horizontal axis ($y = 0$) is assumed.

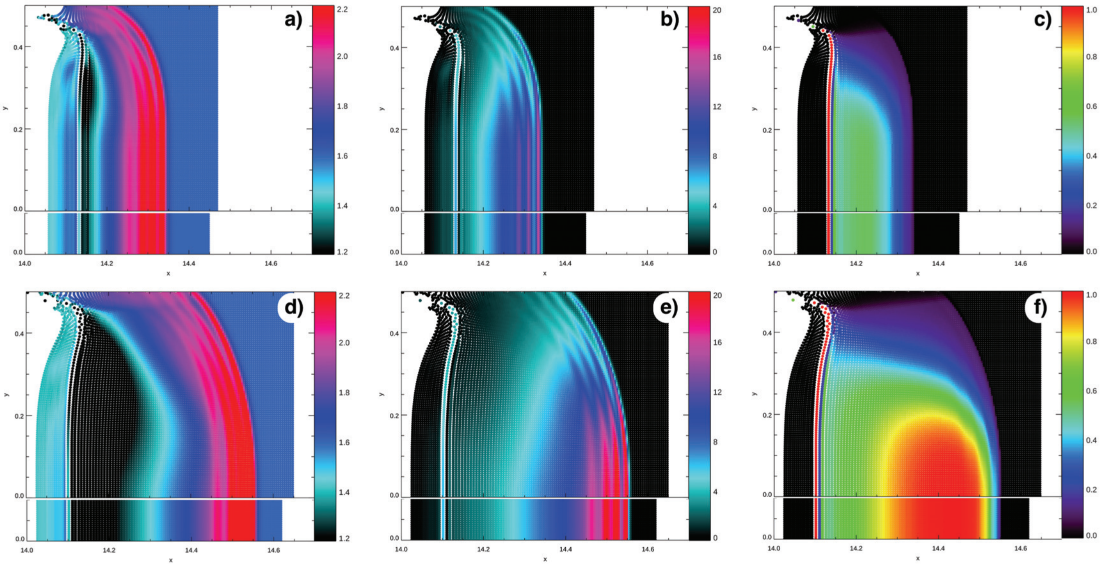

Figure 6.10 *Simulation results of a 75 μm thick and 800 μm wide Kapton flyer impacting HNS-IV modelled in 3D. Results are shown 0.05 μs (top row) and 0.09 μs (bottom row) after impact. The panels show the density (panels* **a** *and* **d***), the pressure (panels* **b** *and* **e***), and the burn ratio (panels* **c** *and* **f***). Each panel is split in two, with the lower part showing the result for a flyer with infinite width for comparison.*

With the flyer width set to 800 μm, the rarefaction from the flyer edge does not reach the symmetry line until well after $t = 0.09$ μs. This is confirmed by the good match between the 3D solution close to the symmetry axis and the 1D solution. From $t = 0.05$ μs to $t = 0.09$ μs, maximum burn ratio in the ignitation front has increased from about 0.5 to 1.0. This confirms that the critical flyer velocity in this case is substantially smaller than the simulated flyer velocity of 2.5 km/s. At $t = 0.05$ μs, we still can see that the pressure and density levels at the shock front, in front of the ignition front, fit well with analytical values obtained from simplified Hugoniot theory (Cooper, 2018).

When the flyer width is reduced to 600 μm, we see from Fig. 6.11 that the rarefaction from the flyer edge is still about 100 μm away from the symmetry axis 0.05 μs after impact. This corresponds to a rarefaction wave propagation speed of roughly 4 km/s which fits well with the sound speed in the post-shock HNS. Where the rarefaction wave has propagated through the pellet, only a small fraction of the explosive has ignited. Closer to the symmetry axis, the burn ratio has at this point in time reached roughly 50%. At $t = 0.09$ μs, the rarefaction waves have reached the symmetry axis and the difference between the 1D solution and the solution with flyer width 600 μm has increased. The region where the burn ratio exceeds 80% is notably smaller in the 3D case than in the 1D case. Still, the burn ratio reaches a sufficiently high level early enough, before the density drops off due to rarefaction, that the ignition process manages to continue and full detonation is eventually achieved. The critical flyer velocity is in this case estimated numerically to be around 2.5 km/s, and this is within the combined accuracy of the experimental and numerical results.

As the flyer width is reduced further, the difference between the 3D solution and the 1D solution becomes ever more apparent. When the flyer width is set to 200 μm, the edge effect is strong even

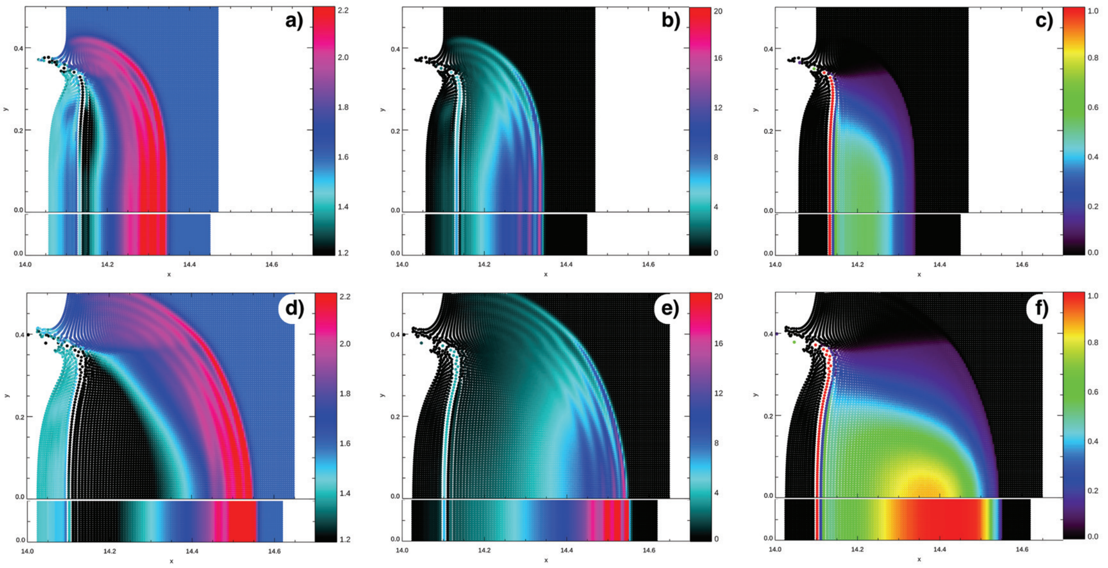

Figure 6.11 *Simulation results of a 75 µm thick and 600 µm wide Kapton flyer impacting HNS-IV modelled in 3D. Results are shown 0.05 µs (top row) and 0.09 µs (bottom row) after impact. The panels show the density (panels* **a** *and* **d***), the pressure (panels* **b** *and* **e***), and the burn ratio (panels* **c** *and* **f***). Each panel is split in two, with the lower part showing the result for a flyer with infinite width for comparison.*

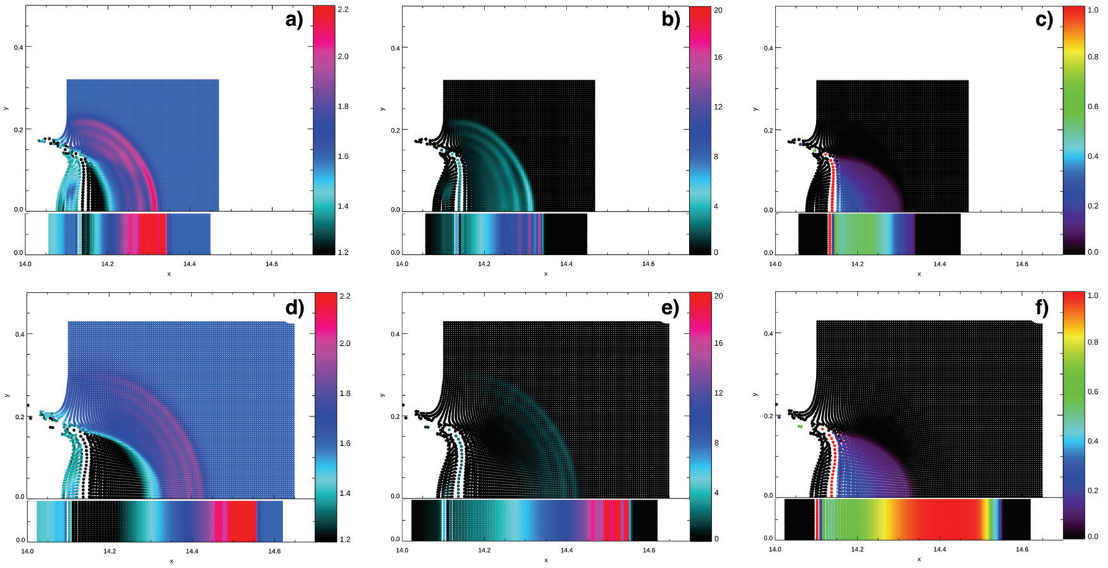

Figure 6.12 *Simulation results of a 75 µm thick and 200 µm wide Kapton flyer impacting HNS-IV modelled in 3D. Results are shown 0.05 µs (top row) and 0.09 µs (bottom row) after impact. The panels show the density (panels* **a** *and* **d***), the pressure (panels* **b** *and* **e***), and the burn ratio (panels* **c** *and* **f***). Each panel is split in two, with the lower part showing the result for a flyer with infinite width for comparison.*

as early as after 0.05 μs, as can be seen in the top row of panels in Fig. 6.12. The shock front is elliptical instead of almost planar, and the burn ratio is not more than 10-20%. This has not changed notably at 0.09 μs. In fact, the shock front peak pressure has dropped considerably from the first to the second snapshot. This indicates that the conditions for detonation are not met in this case. Even when the impact velocity is increased considerably, the numerical solution of this flyer impacting an HNS pellet does not lead to full detonation. This is because the density drops too fast behind the shock front. Increasing the impact velocity only increases the rate at which the density behind the shock front drops. In contrast to what the experimental data suggests, the 75 μm thick and 200 μm wide flyer cannot cause the HNS-IV pellet detonate according to the numerical model.

7 Conclusion

In this report, we have investigated the numerical modelling of short pulse shock initiation of ultrafine Hexanitrostilbene (HNS) using the numerical method Smoothed Particle Hydrodynamics (SPH). An introduction to the numerical method has been given. The ignition process is described using the ignition and growth model proposed by Lee & Tarver (1980) and first applied to HNS by Tarver & Chidester (2014). The adaption of the model to SPH has been described in this report. The 1D results are found to be consistent with experimental and theoretical results from the literature when the numerical resolution is sufficiently large. It appears the resolution requirement is linked to the flyer thickness, with a flyer thickness-to-particle spacing ratio of between 20-40 for acceptable resolution in the 1D case. Simulating the impact of very thin flyers are therefore particularly challenging. Ignition model parameters for ultra-thin flyers needed to be slightly different than the parameters published in Tarver & Chidester (2014). More work is needed in order to determine which parameters are more correct from an analytical point of view.

The current work was done using an in-house simulation code called REGULUS. This code can so far only be run on a single CPU, and this limits the possibilities of using the code for complex problems in 2D and 3D with very high resolution. However, the code has several features which enables problem-specific optimization of the numerical description. Given the strict resolution requirements formulated for the flyer-pellet interaction, two different options were considered for reducing the CPU load while maintaining an acceptable resolution. Due to the unstable nature of the ignition model, it was found that the best strategy for achieving an effective numerical description was to apply an inflow and outflow technique which limits the simulation efforts to a region which contains the shock front and the ignition front, both with sufficient margins. It was shown that in a 2D scenario, the CPU time is reduced to about 1/3 with negligible change in simulation results by applying dynamic inflow and outflow.

Finally, we have compared simulation results for Kapton flyers with thickness 75 μm impacting HNS-IV with experimental data (Bowden, 2018). In particular, the dependence of the critical flyer velocity on the flyer width is studied. Both 2D and 3D results confirm that the numerical results fit the experimental results well when the flyer width is no less than approximately 600 μm. For smaller values of the flyer width, the critical velocity increases faster in the simulations than in the experiments. More work is clearly needed in order to determine the cause of this discrepancy. However, we can point to at least 4 likely candidates which may contribute to the observed differences. First, relevant details concerning the experimental setup have been omitted from the publication (Bowden, 2018). This includes details about the properties of the explosive material, level of shock wave reflections inside the test chamber, and the distance the flyers propagate before impact with the pellet. Secondly, the bridge foil plasma is not included in the simulations and therefore the pressure exerted by the plasma on the flyer is not included. It is reasonable to assume that the accelerating pressure on the flyer could be in the order of several GPa even during impact. This could have a noticeable effect on the results, but would be highly dependent on the distance the flyer needs to move before impacting the pellet. Thirdly, the numerical resolution could be more crucial as we reduce the flyer diameter leading to an increased overestimation of the critical velocity. And finally, fundamental problems in handling elastic problems in SPH could render the method less suited to simulating thin flyers with small to moderate diameter.

References

Børve, S. **Third-generation RSPH in 3D**, 7th SPHERIC Workshop, Prato, Italy, 7, 361-369, 2012.

Børve, S., Omang, M. & Trulsen, J. **Multidimensional MHD shock tests of regularized smoothed particle hydrodynamics**, Astrophys. J., 652, 1306-1317, 2006.

Børve, S., Omang, M. & Trulsen, J. **Regularized smoothed particle hydrodynamics: a new approach to simulating magnetohydrodynamic shocks**, Astrophys. J., 561, 82-93, 2001.

Bowden, M.D. **A volumetric approach to shock initiation of hexanitrostilbene and pentaerythritol tetranitrate**, AIP Conf. Proc., 1979, 150004/1-4, 2018.

Bowden, M.D., Maisey, M.P. & Knowles, S.L. **Shock initiation of hexanitrostilbene at ultra-high shock pressures and critical energy determination**, AIP Conf. Proc., 1426, 615-618, 2012.

Capone, T. et al. **Accuracy and stability of numerical schemes in SPH**, 2nd SPHERIC Workshop, Madrid, Spain, 2, 156-160, 2007.

Clutter, J.K. & Belk, D. **Simulation of detonation wave interaction using ignition and growth**, Shock Waves, 12, 251-263, 2002.

Cooper, P.W. **Explosives Engineering (4th Ed.)**, Wiley-VCH, New York, 2018.

Damm, D. & Dudley, E. **Characterization of physical processes during thin-pulse initiation of energetic materials**, Sandia National Labs., NM (USA), SAND2010-1528C, 1-11, 2010.

Dupont™, **Dupont™ Kapton® - Summary of Properties**, *www.dupont.com/content/dam/dupont/amer/us/en/products/ei-transformation/documents/El-10142-Kapton-Summary-of-Properties.pdf*, 2021

Gingold, R.A. & Monaghan, J.J. **Smoothed particle hydrodynamics: theory and application to non-spherical stars**, Mon. Not. R. Astron., 181, 375-389, 1977.

Kipp, M.E. & Setchell, R.E. **A shock initiation model for fine-grained hexanitrostilbene**, Sandia National Labs., NM (USA), SAND-88-2385C, 209-217, 1988.

Kittell, D.E. **Addressing the gap between meso(grain) and continuum scales with stochastic burn models and probability function theory**, AIP Conf. Proc., 2272/070020, 1-10, 2020.

Kury, J.W., Breithaupt, R.D. & Tarver, C.M. **Detonation waves in Trinitrotoluene**, Shock Waves, 9, 227-237, 1999.

Lee, E.L. & Tarver, C.M. **Phenomenological model of shock initiation in heterogeneous explosives**, Phys. Fluids, 23, 2362-2372, 1980.

Lemons, D.S. & Lund, C.M.. **Thermodynamics of high temperature, Mie-Grüneisen solids**, Am. J. Phys., 67, 1105-1108, 1999.

May, C.M. & Tarver, C.M. **Modeling Short Shock Pulse Duration Initiation of LX-16 and LX-10 Charges**, APS Shock Compression of Condensed Matter, Nashville, TN, USA, 1195, 275-278, 2009.

Monaghan, J.J. **Smoothed particle hydrodynamics**, Rep. Prog. Phys., 68, 1703-1759, 2005.

Monaghan, J.J. **SPH without tensile instability**, J. Comput. Phys., 159, 290-311, 2000.

Monaghan, J.J. & Gingold, R. **Shock simulation by the particle method SPH**, J. Comput. Phys., 52, 374-389, 1983.

Morris, J.P. & Monaghan, J.J. **A switch to reduce SPH viscosity**, J. Comput. Phys., 136, 41-50, 1997.

Moxnes, J.F. & Børve, S. **Simulation of natural fragmentation of rings cut from warheads**, Defence Technology, 11, 319-329, 2015.

Pahl, R.J. et al. **Diameter effects on detonation performance of HNS and CL-20**, 13th Int. Detonation Symp., Sandia Nat. Lab.: Alexandria, VA, USA, 2006.

Price, D.J. **Modelling discontinuities and Kelvin-Helmholtz instabilities in SPH**, J. Comput. Phys., 227, 10040-10057, 2008.

Schwarz, A.C. **Shock initiation sensitivity of hexanitrostilbene (HNS)**, Proc. 7th Symp. (Int.) Detonation, 7, 1024-1028, 1981.

Stewart, D.S. **Lectures on detonation physics: Introduction to the theory of detonation shock dynamics**, Report WL-TR-94-7089, Univ. of Illinois, Urbana Illinois, 1993.

Tarver, C.M. & Chidester, S.K. **Ignition and growth modeling of short pulse shock initiation experiments on fine particle Hexanitrostilbene (HNS)**, J. Phys. Conf. Ser., 500/052044, 1-6, 2014.

Tarver, C.M. & May, C.M. **Short pulse shock initiation experiments and modeling on LX-16, LX-10, and ultrafine TATB**, 14th Int. Detonation Symp., ONR-351-10-185, 648-654, 2010.

Wang, G. et al. **A 3D smoothed particle hydrodynamics method with reactive flow model for the simulation of ANFO**, Propellants, Explosives, Pyrotechnics, 40, 566-575, 2015.

Wendland, H. **Piecewise polynomial, positive definite and compactly supported radial functions of minimal degree**, Adv. Comput. Math., 4, 389-396, 1995.

Yang, G. et al. **Feasibility analysis of SPH method in the simulation of condensed explosives detonation with ignition and growth model**, Comput. & Fluids, 88, 51-59, 2013.

Yarrington, C.D., Wixom, R.R. and Damm, D.L. **Shock interactions with heterogeneous energetic materials**, J. Appl. Phys., 123/105901, 1-20, 2018.

A Low-density correction to the JWL Equation-of-state (EOS)

SPH is a particle method where there is no strict coupling between neighbouring particles, even if the particles initially belong to the same solid object. Only the local forces determine the dynamics of the particles. An advantage of such a method is that fracture can easily be modelled. On the other hand, such a method might in some cases overestimate the break-up of a solid material. Likewise, SPH can sometimes overestimate the drop in density during fracture. As mentioned in section 2.4.1, the HNS-IV density can drop below the equilibrium density when impacted by a high-velocity, thin flyer. In this appendix, we investigate the properties of the JWL EOS for unreacted and reacted HNS-IV identifying an issue with the sound speed in the low-density regime. Then we propose a correction to the standard JWL formulation which secures a real sound speed even at low densities while not affecting the sound speed for densities above or around the equilibrium density.

A.1 Unphysical sound speed in low-density HNS-IV

The sound speed of a material, C_s is calculated from the equation

$$C_s^2 = \frac{dP}{d\rho}. \tag{A.1}$$

In general, P will vary both because of direct dependence on the density ρ, but also indirectly due to changes in specific internal energy (or equivalently in temperature). From the first law of thermodynamics at constant entropy, we have

$$\frac{\partial e}{\partial \rho} = \frac{P}{\rho^2}. \tag{A.2}$$

Eq. A.1 can therefore, in combination with Eq. A.2, be rewritten as

$$C_s^2 = \frac{\partial P}{\partial \rho} + \frac{P}{\rho^2}\frac{\partial P}{\partial e}. \tag{A.3}$$

We want to use this equation to determine the sound speed to first an unreacted explosive and then afterwards to a mix of unreacted and reacted explosive.

A.1.1 Sound speed in the single-component JWL model

In section 2.4.1, we expressed the thermal pressure according to the JWL EOS for a single-component explosive as a function of $\mu = \rho/\rho_0$ and e by Eq. 2.41 as

$$P_{\text{JWL}} = G(\mu) + H(\mu)\rho e, \tag{A.4}$$

where $G(\mu)$ and $H(\mu)$ is given by Eqs. 2.39 and 2.40, respectively. Applying Eq. A.4 to Eq. A.3, we get the following expression for the explosive sound speed squared:

$$C_{s,\text{JWL}}^2 = \frac{1}{\rho_0}\left[\frac{\partial G(\mu)}{\partial \mu} + 2\omega\rho e + \omega P_{\text{JWL}}\right], \tag{A.5}$$

where

$$\frac{\partial G(\mu)}{\partial \mu} = A\left(\frac{R_1}{\mu^2} - \frac{\omega}{\mu} - \frac{\omega}{R_1}\right)e^{-R_1/\mu} + B\left(\frac{R_2}{\mu^2} - \frac{\omega}{\mu} - \frac{\omega}{R_2}\right)e^{-R_2/\mu} + \omega E_0. \tag{A.6}$$

For later comparison with the case where we have a mix of unreacted and reacted explosive material, we want to rewrite Eq. A.5 by reintroducing the quantity $S(\mu)$ defined in Eq. 2.46, which in the single-component case can be written simply as

$$S(\mu) = \frac{1}{H(\mu)} = \frac{\rho_0}{\omega\rho}. \tag{A.7}$$

Also, we can eliminate the direct reference to e by noting that

$$\omega\mu e = -\frac{G(\mu)}{\rho} + \frac{P_{\text{JWL}}}{\rho}. \tag{A.8}$$

By rearrange the terms and applying Eqs. A.7 and A.8, the explosive sound speed squared can be written as

$$C_{s,\text{JWL}}^2 = \frac{1}{\rho S}\left[(2S+1)P_{\text{JWL}} - 2SG\right] + \frac{1}{\rho_0}\frac{\partial G(\mu)}{\partial \mu}. \tag{A.9}$$

A.1.2 Sound speed in the multi-component JWL model

For a fluid mix where the thermodynamical response of each component is described by a JWL EOS, and where pressure equilibrium is assumed, the pressure is expressed as

$$P = \frac{1}{S(\mu)}\left[\rho e + \sum_i s_i(\mu) G_i(\mu)\right], \tag{A.10}$$

as explained in section 2.4.1. The quantities $s_i(\mu)$ and $S(\mu)$ are defined by Eqs. 2.45 and 2.46, respectively. The derivatives of $s_i(\mu)$ and $1/S(\mu)$ with respect to the density ρ are given by:

$$\frac{ds_i}{d\rho} = -\frac{s_i}{\rho} \tag{A.11}$$

and

$$\frac{dS^{-1}}{d\rho} = \frac{1}{\rho S}. \tag{A.12}$$

$$\tag{A.13}$$

Combining Eqs. A.10-A.12 with Eq. A.3, we get the following expression for the multi-component JWL sound speed squared:

$$C_{s,\text{MJWL}}^2 = \frac{1}{\rho S}\left[(2S+1)P_{\text{MJWL}} - 2\sum_i s_i G_i\right] + \frac{1}{\rho_0 S}\sum_i s_i \frac{\partial G_i}{\partial \mu}. \tag{A.14}$$

This is then the multi-component equivalent to the expression in Eq. A.9.

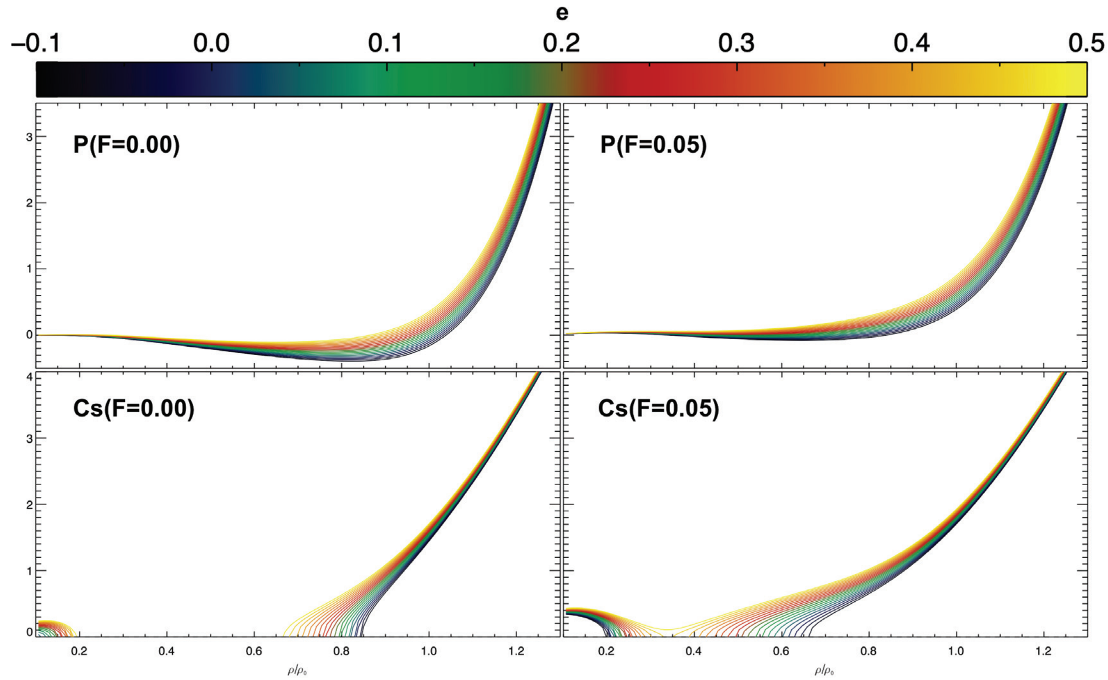

Figure A.1 *Dual-component JWL EOS for HNS-IV: Pressure in GPa (P) and sound speed in km/s (C_s) plotted as function of normalised density, μ, for burn ratios $F = 0.0$ and $F = 0.05$. The curve colours indicate the thermal energy, e, in units of kJ/g.*

A.1.3 Determining the physical validity of the HNS-IV dual-component JWL model

In order for Eq. A.14 to be a valid expression for the sound speed squared, the right-hand side of the equation must be positive. This implies that the pressure must always increase when the density increases. With the parameters chosen for unreacted HNS, the condition for validly defined sound speed is not guaranteed. This can therefore represent a problem in the description of HNS-IV when the reaction ratio is less than roughly 10%. Fig. A.1 shows the pressure, P, and sound speed, C_s, as functions of normalised density for unreacted HNS-IV ($F = 0.0$) and HNS-IV with 5% reaction ratio ($F = 0.05$). The curve colours indicate the thermal energy, e, in units of kJ/g. We see that for the unreacted case, the pressure drops off monotonously with dropping density until the normalised density reaches roughly 0.8. At the same time, the sound speed drops off almost linearly. Depending on the thermal energy, the sound speed reaches zero for normalised density somewhere between 0.65 and 0.85, and the sound speed is mostly undefined for densities below this critical value. Once a fraction of the HNS-IV has reacted, the density interval where the sound speed is undefined decreases. With a burn ratio of 5% and roughly zero thermal energy, the density interval where the sound speed is undefined has been reduced to be roughly between 0.2 and 0.6.

A.2 Corrected Jones-Wilkins-Lee (CJWL) formulation

As discussed in section 2.4.1, a small number of SPH particles representing part of the HNS-IV pellet can experience density levels well below unity during a flyer impact simulation. In some cases, this can bring particles into a state where the expression for the sound speed squared is negative when the standard multi-component JWL model is used. To avoid this problem altogether, a low-density and low-temperature correction to the EOS, hereafter referred to as the **corrected JWL** model, is proposed. The ambition is not to provide an accurate description of the explosive material in the low-density, low-temperature regime since this is not a very important regime in the current application. Instead, the aim is to avoid a numerical problem which could otherwise cause simulations to crash. Assuming the EOS can still be written on the form given by Eq. 2.41 and that the term dependent on thermal energy is unchanged, the corrected model is constructed by replacing the term $G(\mu)$ defined in Eq. 2.39, by a simple, monotonous term below a certain, critical density level, μ_L. The corrected $G(\mu)$ function is given as

$$G(\mu) = \begin{cases} G_{\text{JWL}}(\mu) & \text{if } \mu \geq \mu_L; \\ G_L(\mu) & \text{if } \mu < \mu_L, \end{cases} \tag{A.15}$$

where we define $G_L(\mu)$

$$G_L(\mu) = G_{\text{JWL}}(\mu_L) \left(\frac{\mu_L}{\mu} \right)^k . \tag{A.16}$$

The constant $G_{\text{JWL}}(\mu_L) < 0$ secures continuity for $G(\mu)$ at the critical density μ_L, and because the constant is negative, $G_L(\mu)$ will monotonously decreasing with decreasing density if $k > 0$. For simplicity, we choose $k = 1$ in this work.

Another reasonable constraint that the corrected JWL formulation should fulfil, is that the sound speed should be continuous at $\mu = \mu_L$. As a consequence of this requirement, μ_L is no longer a free parameter. To determine μ_L, we start with the condition

$$\frac{\partial G_{\text{JWL}}(\mu_L)}{\partial \mu} = \frac{\partial G_L}{\partial \mu}, \tag{A.17}$$

where $\partial G_{\text{JWL}}/\partial \mu$ is given by Eq. A.6 and

$$\frac{\partial G_L(\mu)}{\partial \mu} = -k \frac{G_{\text{JWL}}(\mu_L)}{\mu_L} \left(\frac{\mu_L}{\mu} \right)^{k+1} . \tag{A.18}$$

Insert the expression for $G_{\text{JWL}}(\mu)$ from Eq. 2.39 and rearranging the terms, we get the following non-linear equation where μ_L is the free variable:

$$Q(\mu_L) = 0 \tag{A.19}$$

with

$$\begin{aligned} Q(\mu_L) \quad = \quad & A \left(R_1 + (k - \omega)\mu_L - (k+1)\frac{\omega \mu_L^2}{R_1} \right) e^{-R_1/\mu_L} \\ & + B \left(R_2 + (k - \omega)\mu_L - (k+1)\frac{\omega \mu_L^2}{R_2} \right) e^{-R_2/\mu_L} + (k+1)\omega \mu_L^2 E_0. \end{aligned} \tag{A.20}$$

This equation can easily be solved numerically with a few Newton-Raphson iterations. For the material parameters of unreacted HNS-IV, we find $\mu_L = 0.850$.

The modification to the function $G(\mu)$ is in the case of HNS-IV only applied to the unreacted EOS, while the reacted EOS is left unchanged. With these minor adjustments, Eqs. 2.47 and 2.50

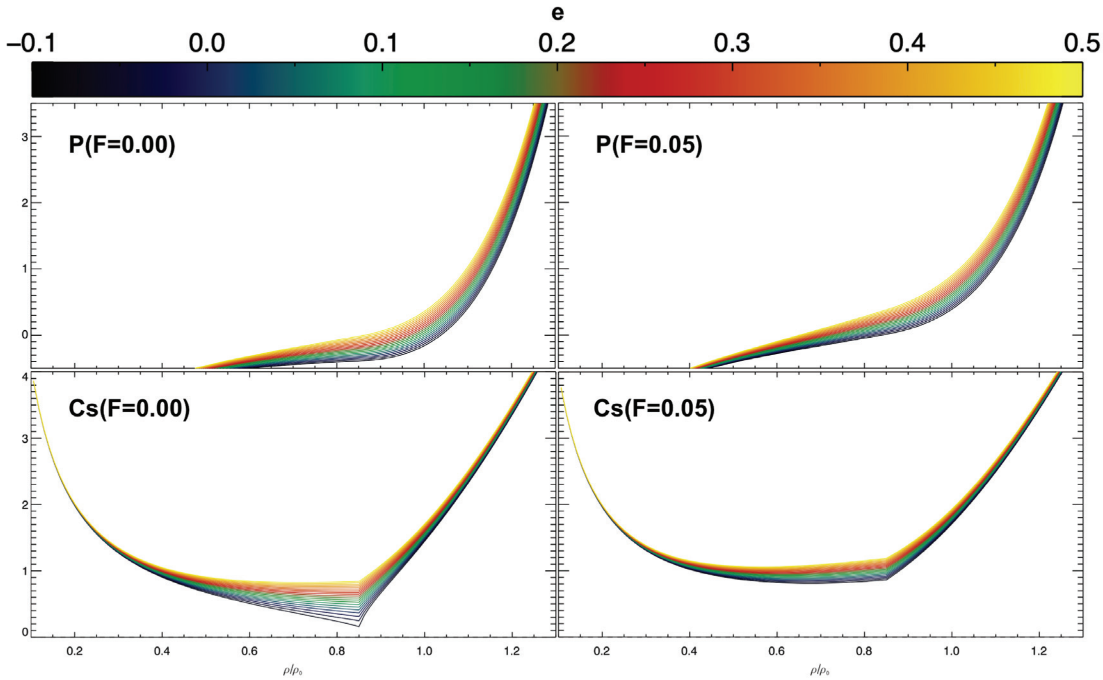

Figure A.2 Corrected dual-component JWL EOS for HNS-IV with $G_L(\mu)$ given by Eq. A.16: Pressure in GPa (P) and sound speed in km/s (C_s) plotted as function of normalised density, μ, for burn ratios $F = 0.0$ and $F = 0.05$. The curve colours indicate the thermal energy, e, in units of kJ/g.

for the pressure and sound speed in the mix of reacted and unreacted HNS-IV is still valid. Fig. A.2 shows the pressure, P, and sound speed, C_s, as functions of normalised density for unreacted HNS-IV ($F = 0.0$) and HNS-IV with 5% reaction ratio ($F = 0.05$) when using the corrected EOS. The curve colours once again indicate the thermal energy, e, in units of kJ/g. Fig. A.1 is therefore directly comparable to Fig. A.1. We see that for normalised density above 0.85 or so the two models are identical. However in the low-density regime, the pressure drops off more quickly with decreasing density. The sound speed has a minimum at $\mu = \mu_L$ and then increases with decreasing density, initially quite slowly but later on quite rapidly, as the density approaches 0. This EOS, which is used throughout this work, secures a smooth material response in cases where the normalised density drops below μ_L.

A.2.1 Alternative form of the low-density correction

One undesirable side-effect of using the corrected JWL EOS when $G_L(\mu)$ is defined by Eq. A.16, is that the sound speed increases rapidly when $\mu \ll 1$ and actually becomes infinite when $\mu = 0$. This is indicated in the bottom panels of Fig. A.2 by the sharp rise in sound speed as the normalised density drops below 0.3 or so. An alternative form of $G_L(\mu)$ which removes this particular problem, was derived near the end of this study. Since changing the functional of G_L turned out to have negligible impact on the simulation results presented here, the original form of G_L has been used throughout this report. For completeness, the alternative form of $G_L(\mu)$, how it is derived and what the inert EOS will look like in this case, is presented briefly here.

We restrict this discussion to the inert case. If we combine Eqs. A.4 and A.5 and only consider the zero-temperature case ($e = 0$), we can express P and C_s^2 as functions of $G(\mu)$ only:

$$P_{\text{JWL}} = G(\mu) \tag{A.21}$$

and

$$C^2_{s,\text{JWL}} = \frac{1}{\rho_0}\left[\frac{\partial G(\mu)}{\partial \mu} + G(\mu)\right]. \tag{A.22}$$

Again, we require that the low-density correction to the EOS, represented by the function $G_L\mu$ must be chosen so as to secure continuity of both pressure and sound speed at the critical density level μ_L. From Eq. A.21 we get

$$G_L(\mu_L) = G_{\text{JWL}}(\mu_L) \equiv G_L \tag{A.23}$$

and from Eq. A.22 we get

$$G_L(\mu_L) + \frac{\partial G_L(\mu_L)}{\partial \mu} = G_{\text{JWL}}\mu_L(\mu_L) + \frac{\partial G_{\text{JWL}}(\mu_L)}{\partial \mu} \equiv F_L. \tag{A.24}$$

Instead of the polynomial form given by Eq. A.16, we now propose that $G_L(\mu)$ should have an exponential form:

$$G_L(\mu) = A_L e^{R_L \mu}. \tag{A.25}$$

In this case, the user must choose the critical density μ_L. Then, by combining Eqs. A.23-A.4, we can determine the constants A_L and R_L as

$$R_L = \frac{F_L}{G_L} - 1 \tag{A.26}$$

and

$$A_L = \frac{G_L}{e^{R_L \mu_L}}. \tag{A.27}$$

As before, it is appropriate to choose $\mu_L = 0.85$. Fig. A.3 shows the pressure (top panels) and sound speed (bottom panels) for the inert case (left panels) and the case with 5% burn ratio (right panels), with different values of the internal energy. It can be seen that the pressure is more sensitive to changes in density when $\mu > \mu_L$. For $\mu < \mu_L$, the pressure is roughly a linear function of μ. This causes the sound speed in the low-density regime to become almost independent of the density. In contrast, using the original correction term (see Eq. A.16) the sound speed is strongly sensitive to changes in the density in the low-density regime.

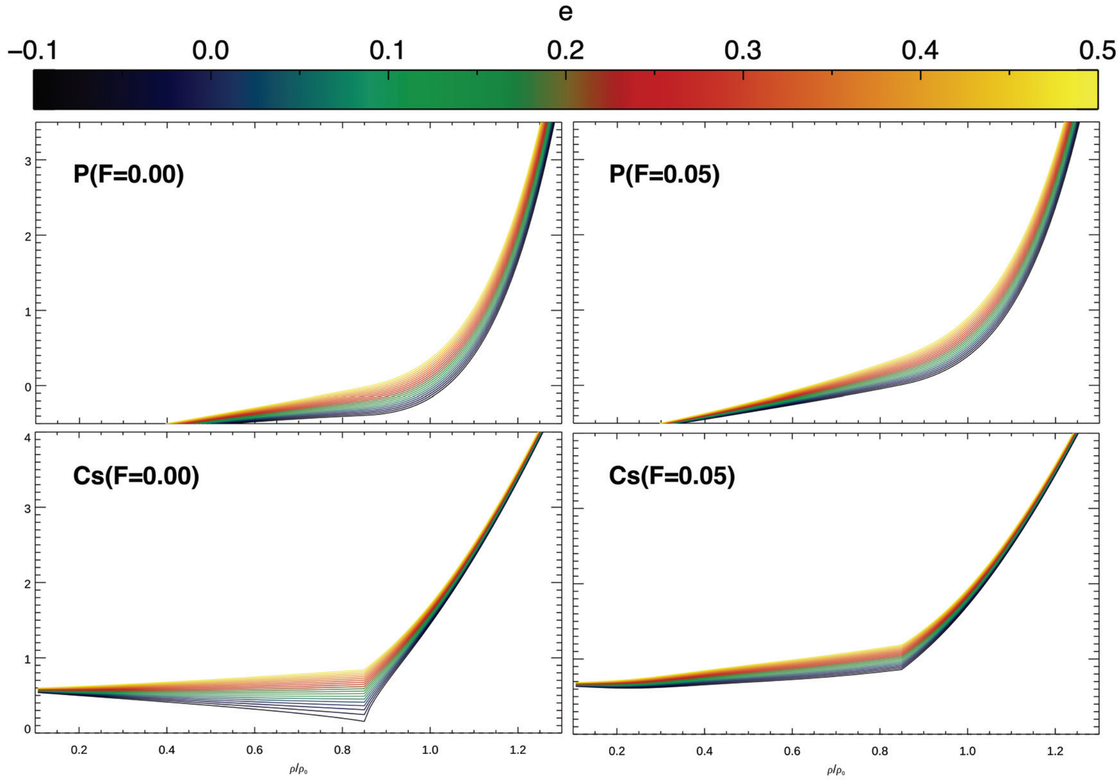

Figure A.3 *Corrected dual-component JWL EOS for HNS-IV with $G_L(\mu)$ given by Eq. A.25: Pressure in GPa (P) and sound speed in km/s (C_s) plotted as function of normalised density, μ, for burn ratios $F = 0.0$ and $F = 0.05$. The curve colours indicate the thermal energy, e, in units of kJ/g.*

About FFI

The Norwegian Defence Research Establishment (FFI) was founded 11th of April 1946. It is organised as an administrative agency subordinate to the Ministry of Defence.

FFI's mission

FFI is the prime institution responsible for defence related research in Norway. Its principal mission is to carry out research and development to meet the requirements of the Armed Forces. FFI has the role of chief adviser to the political and military leadership. In particular, the institute shall focus on aspects of the development in science and technology that can influence our security policy or defence planning.

FFI's vision

FFI turns knowledge and ideas into an efficient defence.

FFI's characteristics

Creative, daring, broad-minded and responsible.

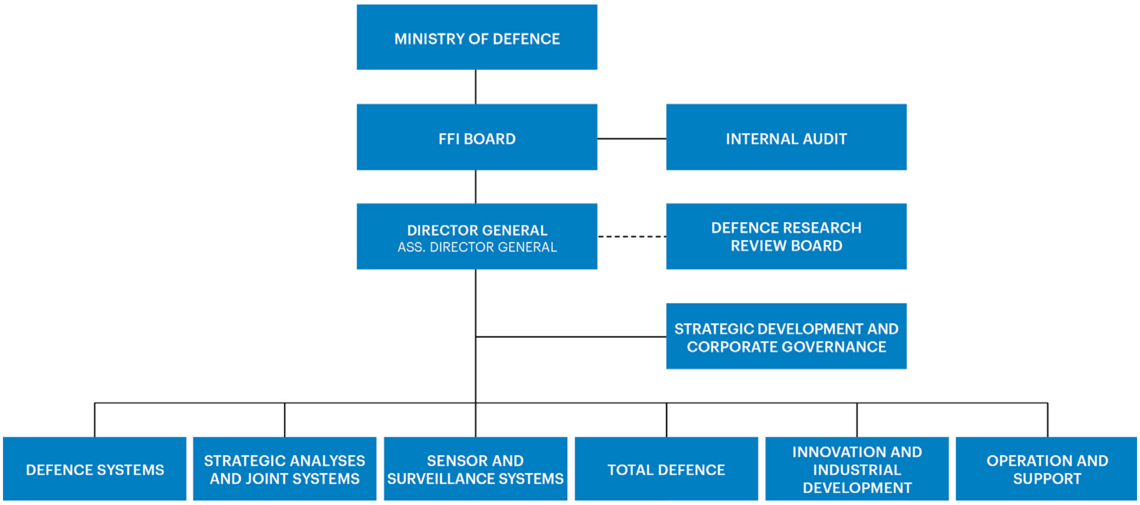

Forsvarets forskningsinstitutt (FFI)
Postboks 25
2027 Kjeller

Besøksadresse:
Kjeller: Instituttveien 20, Kjeller
Horten: Nedre vei 16, Karljohansvern, Horten

Telefon: 91 50 30 03
E-post: post@ffi.no
ffi.no

Norwegian Defence Research Establishment (FFI)
PO box 25
NO-2027 Kjeller
NORWAY

Visitor address:
Kjeller: Instituttveien 20, Kjeller
Horten: Nedre vei 16, Karljohansvern, Horten

Telephone: +47 91 50 30 03
E-mail: post@ffi.no
ffi.no/en